Journal of Materials Chemistry A

ROYAL SOCIETY OF CHEMISTRY

REVIEW

View Article Online
View Journal | View Issue

Check for updates

Cite this: J. Mater. Chem. A, 2024, 12, 27825

# Recent trends in $CO_2$ electroreduction over metal–organic framework-derived materials: a comprehensive review

Nadia Gholampour,*[a] Chizoba I. Ezugwu,[b] Hussein A. Younus, *[ce] Damien P. Debecker, [a] Mohamed Al Abri, [cd] Rashid Al hajri,[d] Chih-Ming Kao[f] and Francis Verpoort *[ghi]

Carbon dioxide reduction through electrochemical energy is an emerging and appealing approach towards $CO_2$ mitigation, and it is a potential technique in which the current and faradaic efficiencies can be optimized for the efficient/effective conversion of $CO_2$ to solar fuel (storable high-density chemical energy). However, a challenge associated with the current state-of-the-art electrocatalytic systems is developing efficient, selective, and cost-effective heterogeneous catalysts. In this case, materials derived from metal–organic frameworks (MOFs) are promising electrocatalysts that not only possess porous structures similar to their parent MOFs but are also endowed with improved stability and conductivity, which are required in the $CO_2$ reduction reaction ($CO_2$RR). This review surveys the updated strategies to rationally design efficient MOF-based electrocatalysts and MOF-derived materials for $CO_2$ reduction. Various MOF-derived materials are comprehensively discussed, together with the strategies aimed at improving product selectivity. Furthermore, active sites and detailed underlying mechanisms of $CO_2$ reduction are discussed to gain better insights into the future development of electrocatalysts. This investigation aims to highlight the recent advances in the $CO_2$RR to inspire the development of new techniques in designing electrocatalysts based on MOF structures with high performance and high stability.

Received 21st May 2024
Accepted 22nd August 2024

DOI: 10.1039/d4ta03502j

rsc.li/materials-a

Published on 25 August 2024. Downloaded on 02.05.26 08:00:32.

## 1. Introduction

Despite the development of various types of renewable energy sources, fossil fuels remain one of the widely used energy sources, resulting in the emission of a massive amount of $CO_2$ into the atmosphere annually.[1,2] One of the leading causes of climate change is $CO_2$ emissions, resulting in a record high $CO_2$ concentration of 420.2 ppm in the atmosphere in 2023. It is known that this increase in atmospheric $CO_2$ has led to an enhancement in Earth's average temperature, which is associated with various forms of environmental disasters, including severe hurricanes and ecosystem destruction. There are two main approaches to decrease the levels of atmospheric $CO_2$: (1) restricting the combustion of fossil resources while curbing the energy demand and using cleaner energy sources, including solar and wind energy (however, their storage is a severe concern in this approach) and (2) capturing and utilizing $CO_2$ to produce other valuable chemicals. The latter approach has drawn the attention of numerous researchers for applying several techniques to fix $CO_2$ into fine chemicals, including photochemical reduction,[3–6] biological transformation,[7] chemical reduction,[8–10] and electrochemical reduction.[11–13]

In this regard, the electrochemical $CO_2$ reduction reaction ($CO_2$RR) is among the potential techniques in which renewable energy is converted $CO_2$ into valuable chemicals and fuels such as methanol, methane, formic acid, CO, and ethanol.[14–18] It is worth mentioning that many different catalysts, including homogeneous[13,19,20] and heterogeneous[21] catalysts, have been developed to achieve this goal, and undeniably, heterogeneous catalysts are prominent over homogeneous catalysts due to their easy recycling, high stability, and low toxicity. The products of the $CO_2$RR depend on the electrolyte medium, applied

[a]Institute of Condensed Matter and Nanosciences (IMCN), Université Catholique de Louvain (UCLouvain), Place Louis Pasteur, 1, Louvain-la-Neuve, Belgium. E-mail: nadia.gh6183@gmail.com

[b]Centre of Water Technology (WATEC) and Department of Biological and Chemical Engineering, Aarhus University, Universitetsbyen 36, 8000 Aarhus C, Denmark

[c]Nanotechnology Research Center, Sultan Qaboos University, P.O Box 17, Al Khoud, Muscat, PC 123, Oman. E-mail: hay00@fayoum.edu.eg

[d]Petroleum and Chemical Engineering Department, Sultan Qaboos University, P.O Box 17, Al Khoud, Muscat, PC 123, Oman

[e]Chemistry Department, Faculty of Science, Fayoum University, 63514, Egypt

[f]Institute of Environmental Engineering, National Sun Yat-Sen University, Kaohsiung, Taiwan

[g]Joint Institute of Chemical Research (FFMiEN), Peoples Friendship University of Russia (RUDN University), 6 Miklukho-Maklaya Str., 117198 Moscow, Russia

[h]National Research Tomsk Polytechnic University, Lenin Avenue 30, 634050 Tomsk, Russia

[i]State Key Laboratory of Advanced Technology for Materials Synthesis and Processing, Wuhan University of Technology, Wuhan 430070, PR China. E-mail: francis@whut.edu.cn

Published on 25 August 2024. Downloaded on 02.05.26 08:00:32.

potential, and, remarkably, the type of applied electrocatalyst. For instance, it has been proven that Ag and Au are suitable electrocatalysts to produce CO, while the formation of hydrocarbons and oxygenate products (ethanol, methanol, and methane) is achieved over Cu catalysts.[22] Furthermore, numerous metal-free catalysts composed of carbon materials (graphene, carbon nanotubes, nanoporous carbon, and graphene dots) have been shown to be active in the $CO_2$RR.[23–25] In the last two decades, porous frameworks, covalent organic frameworks (COFs),[26–28] metal–organic frameworks (MOFs),[29–31] and materials derived from them[32] have been highlighted as highly promising catalysts for $CO_2$RR.

Metal–organic frameworks (MOFs) are a class of porous polymers that coordinate metal nodes with organic ligands to form a 1D–3D structure. Owing to their large surface area, tunable porosity, and large pore volume by adjusting their metal species or organic linkers, MOFs are recognized as promising materials for many applications, including gas storage/separation, adsorption, water treatment, solar cells, sensing, energy storage (batteries and supercapacitors), catalysis,[33–39] and in particular, (electro)catalysis.[37,38,40–43] However, although several MOFs have been applied in electrochemical $CO_2$RR, issues such as their low conductivity[44,45] and their poor chemical stability in water[46,47] hinder their application for this purpose. In contrast, MOF-derived materials can remarkably overcome these issues, and thus considered more promising candidates. MOF-derived materials have attracted attention due to the dual roles of their metal nodes, which on the one hand, can create metal-active sites, and organic linkers, on the other hand, creating heteroatom (N, S, P, B)-doped carbonaceous materials after pyrolysis. Here, the MOF structure plays an essential role as a self-template for the homogeneous dispersion of heteroatoms and metals through the carbon matrix, the formation of single-atom sites, and also the emergence of porosity inherited from the pristine MOF.[48–52]

This review addresses the recent reported developments on MOF-derived materials employed for electrochemical $CO_2$ reduction. Electrochemical $CO_2$ reduction and the applications of MOF materials are topics of significant interest in recent chemical and material research worldwide. Thus, the record of publications on $CO_2$RR over MOFs and MOF-derived materials is astonishing. Therefore, several excellent reviews were recently published, offering diverse perspectives on this matter.[53–55] However, to present a thorough study of the design and synthesis of MOF-derived materials for enhanced electrochemical $CO_2$ reduction performance, a comprehensive investigation is still required. This review will also discuss the role of active sites and involved mechanisms to gain a better understanding into the design of new electrocatalysts in $CO_2$RR based on MOF materials. This review selectively presents some of the recent advances and pertinent challenges in this field, focusing on MOF-derived materials applied for electrochemical $CO_2$ reduction. Initially, we present an overview of the electrochemical reduction of $CO_2$. In the second section, the pristine MOFs used in $CO_2$RR are briefly discussed, focusing on their role in tuning the micro-environment during $CO_2$RR and their stability. In Section 3, the MOF-based composites employed in electrochemical $CO_2$RR are explored. Finally, in Section 4, the active sites and mechanisms of MOF-derived materials in $CO_2$RR are discussed in detail.

### 1.1 Electrochemical $CO_2$RR

**1.1.1 General proposed mechanisms for electrochemical $CO_2$RR.** $CO_2$RR is a multistep reaction that includes two, four, six, eight, or twelve electron transfer/pathways, as listed in Table 1. During $CO_2$ electroreduction, various reduction products may be generated depending on the characteristics of the catalyst, the applied potential, and the reaction medium. Usually, the $CO_2$RR involves three general steps, as follows: (1) adsorption of $CO_2$ on the electrocatalyst surface (cathode) and the formation of $*CO_2^{\delta-}$ species, (2) cleavage of the C–O bond by electron transfer and/or proton coupling, followed by C–H and C–C bond formation, and (3) product desorption from the surface of the catalyst, which subsequently distributes in the electrolyte.

Understanding the mechanism of $CO_2$ electroreduction has been proven to be challenging due to the need for advanced methods to characterize the intermediates formed during the $CO_2$RR. Moreover, given that $CO_2$RR is a multiple electron/proton transfer reaction, controlling the reaction pathways and product selectivity is difficult. According to the applied potential, various $C_1$ and $C_2$ compounds are formed during this reaction process (Table 1). Owing to the high chemical stability of the $CO_2$ molecule, cleaving the C=O bonds and altering the orientation of the linear $CO_2$ to a bent $*CO_2^{\delta-}$ molecular structure, which has a lower LUMO energy level, requires a significant energy input of about 750 kJ $mol^{-1}$. According to

Table 1 The different possible reactions happening at the cathode in the electroreduction of $CO_2$

| The type of reaction | The number of electrons | The applied potential[a] ($E^0$ (V)) | The possible product |
|---|---|---|---|
| $2H^+ + 2e^- \rightarrow H_2$ | 2 | −0.41 | Hydrogen |
| $CO_2 + 2H^+ + 2e^- \rightarrow HCOOH$ | 2 | −0.61 | Formic acid |
| $CO_2 + 2H^+ + 2e^- \rightarrow CO + H_2O$ | 2 | −0.52 | Carbon monoxide |
| $CO_2 + 4H^+ + 4e^- \rightarrow HCHO + H_2O$ | 4 | −0.51 | Formaldehyde |
| $CO_2 + 6H^+ + 6e^- \rightarrow CH_3OH + H_2O$ | 6 | −0.38 | Methanol |
| $CO_2 + 8H^+ + 8e^- \rightarrow CH_4 + 2H_2O$ | 8 | −0.24 | Methane |
| $2CO_2 + 12H^+ + 12e^- \rightarrow C_2H_4 + 4H_2O$ | 12 | −0.34 | Ethylene |
| $2CO_2 + 12H^+ + 12e^- \rightarrow C_2H_5OH + 3H_2O$ | 12 | −0.33 | Ethanol |

[a] *vs.* Standard hydrogen electrode (SHE) at PH 7 at 25 °C.

 This journal is © The Royal Society of Chemistry 2024

Published on 25 August 2024. Downloaded on 02.05.26 08:00:32.

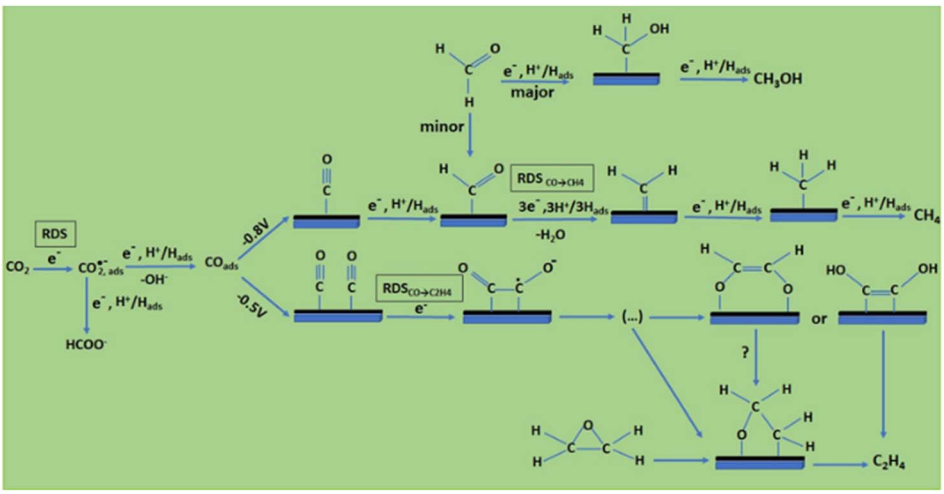


Fig. 1 Suggested mechanism of $CO_2$ electrochemical reduction on copper. Reproduced with permission from ref. 56 Copyright 2011, the Royal Society of Chemistry.

the proposed mechanism of electrochemical reduction of $CO_2$ on the Cu electrode surface (Fig. 1),[56] a high energy barrier is involved in initial adsorption and transferring one electron to $CO_2$ to generate the $*CO_2^{\bullet-}$ intermediate; this step is identified as the rate-determining step (RDS). Although the exact geometry of the chemisorbed $*CO_2^{\delta-}$ species on the catalyst surface is still unknown, the three possible orientations are illustrated in Fig. 2.[57] The reactivity of the $*CO_2^{\bullet-}$ intermediate on the metal surface plays a significant role in the arrangement of the final products. It was shown that the behavior of the $*CO_2^{\bullet-}$ intermediate on the surface of various metals is different, prompting the formation of different products. For example, on the surface of Sn or In, the $*CO_2^{\bullet-}$ intermediate is bound to the metal *via* an oxygen atom, which upon further conversion, will lead to the formation of formate ($HCOO^-$). In contrast, the $*CO_2^{\bullet-}$ intermediate is bound *via* the C atom on the surface of Ag and Au. In this case, *COOH will be formed, which can be reduced to CO.[58] Among the metals studied by Hori *et al.*,[58] Cu was found to be the only metal that can still catalyze $CO_2$ conversion to HCOOH, CO, $CH_4$, and $C_2H_4$. It has been discovered that the main limiting step for hydrocarbon generation is the protonation of CO* to CHO*.[59]

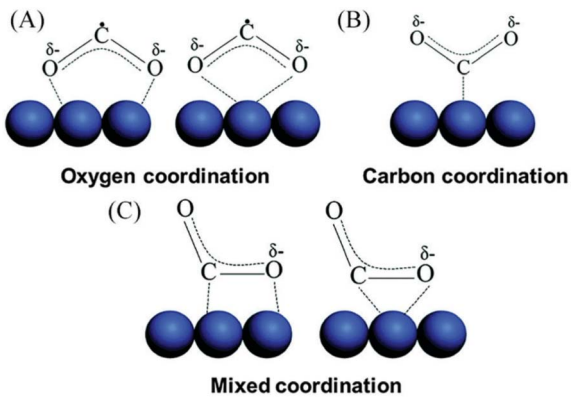


Fig. 2 Illustration of the possible orientation of $CO_2$ on the surface of the electrocatalyst. (a) Oxygen coordination, (b) carbon coordination, (c) mixed coordination. Reproduced with permission.[57] Copyright 2016, the Royal Society of Chemistry.

Considering the structure and pH effects on the reduction products as well as density functional theory (DFT) results, Kortlever *et al.*[15] proposed the mechanism for $CO_2$ reduction on Cu (Fig. 3). The $C_1$ pathway exhibits methane production, where formyl (*CHO) or *COH species is formed as the reduction product of the CO intermediate, which is subsequently reduced to methane. It has been reported that at high overpotentials, intermediate dimerization may lead to ethylene production in the $C_1$ pathway. The dimerization of CO occurs at low overpotentials, which is the $C_2$ pathway and is the rate-determining step for CO reduction by generating a $*C_2O_2^-$ intermediate through the transfer of an electron, explaining the preference for an alkaline medium for reducing CO.

**1.1.2 Electrochemical cell design/components for $CO_2$ reduction.** Generally, an electrocatalytic $CO_2$ reduction reaction takes place in an H-type cell with two compartments separated by either a membrane (*e.g.*, Nafion) or a glass frit under aqueous or non-aqueous conditions, respectively. In the cathodic compartment, which includes the working electrode (where the catalyst is loaded) and the reference electrode (Ag/AgCl), $CO_2$ reduction occurs. Meanwhile, the oxidation reaction, typically oxygen evolution reaction (OER), takes place at the anode surface, *i.e.*, the counter electrode (Pt), when the process is carried out under aqueous conditions.[60,61] Generally, the hydrogen evolution reaction (HER) competes with $CO_2$RR in the cathodic compartment, resulting in a lower faradaic efficiency (FE) for the $CO_2$R products. An H-type cell for $CO_2$RR is schematically presented in Fig. 4. In the H-type cell, the liquid electrolyte facilitates the ionic transport of protons and the reaction environment. Various types of electrolytes, including aqueous[62,63] and non-aqueous electrolytes,[64,65] have been used in most $CO_2$RR studies. The electrolyte pH value, cations, and

Published on 25 August 2024. Downloaded on 02.05.26 08:00:32.

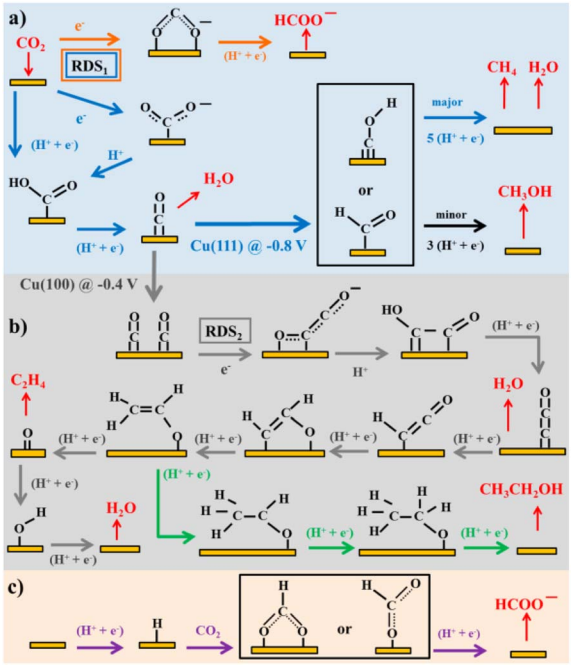


Fig. 3 Plausible $CO_2$ electrocatalytic reduction reaction pathways using transition metals and molecular catalysts: (a) blue arrows show the pathways from $CO_2$ to CO and $CH_4$, black arrows to $CH_3OH$, and orange arrows to $HCOO^-$; (b) grey arrows display the pathways from $CO_2$ to ethylene and green arrows to ethanol; and (c) purple arrows demonstrate the pathway of $CO_2$ insertion into a metal–H bond resulting formate. Adsorbates species are in black, while reactants and products in the solution are in red. Potentials are determined *vs.* RHE. RDS stands for the rate-determining steps and the steps in which either coordinated or separated proton–electron occurs is indicated by $H^+$, $e^-$. Reproduced with permission.[15] Copyright 2015, the American Chemical Society.

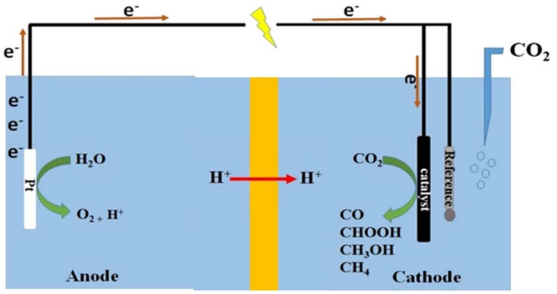


Fig. 4 Schematic of the cell applied in the electrochemical reduction of $CO_2$.

anions are three parameters of aqueous electrolytes that have a great impact on the products of the $CO_2$RR.

Practically, there are two values of pH in an H-type cell, the bulk electrolyte pH and the local pH at the surface of the working electrode. The selectivity and overpotentials in $CO_2$RR are affected by the electrolyte pH. For instance, unlike $C_2H_4$ formation, the production of $CH_4$ is pH-dependent.[66] Therefore, enhanced selectivity for $C_2H_4$ in an alkaline solution and a reduced overpotential could be achieved.[67,68] It has been realized that larger cations such as $Cs^+$ and $K^+$ prompt an increment in the total current density and selectivity towards $H_2$ and $C_2H_4$ production.[64,69] However, the effects of anions have not been studied as much as cations. It was discovered that strongly solvated anions such as $OH^-$ stabilize the rate-limiting $CO_2^-$ intermediate, leading to higher selectivity and lower overpotentials for CO production in comparison with anions such as $Cl^-$ that are less solvated.[66] Alternatively, non-aqueous electrolytes, such as *N*,*N*-dimethylformamide (DMF) and acetonitrile, can also be used for $CO_2$RR, offering the advantages of higher $CO_2$ solubility compared to aqueous conditions and low hydrogen concentration to enhance $CO_2$RR and minimize the competitive HER, respectively.[70,71] However, these electrolytes may interact with the $CO_2$RR pathways differently.[65] In non-aqueous electrolytes, the reaction pathways and reduction products will vary from aprotic to protic solvents, where HER can still be achieved in protic electrolytes, and the electrodes can achieve the formation of hydrocarbon products. Therefore, the choice of electrolyte significantly impacts the product selectivity depending on the capability of the electrolyte to act as a proton source.[71,72]

In real electrolyzers, $CO_2$RR takes place within a gas–liquid–solid triple-phase boundary. However, achieving economic viability is challenging due to the limited mass transfer, product selectivity issues, and high cell voltages at high current densities, which result in significant ohmic losses and electrode overpotentials.[73] Thus, ensuring an adequate supply of gas reactants to the catalyst surface is crucial at higher current densities to sustain high reaction rates.[74,75] Nevertheless, most of the current research emphasizes catalyst materials rather than mass transfer or the microenvironment. Often, the solubility and diffusion of $CO_2$ in the electrolyte limit the rate of $CO_2$ mass transfer, and consequently the overall reaction rate. Increasing the solubility of $CO_2$ can be achieved by operation at high pressure or using a more costly, and often more toxic or corrosive solvent as the electrolyte. Alternatively, a more promising approach to overcoming both the $CO_2$ solubility and diffusion limitations is the use of gas diffusion electrodes (GDEs), which are porous electrodes with a high surface area. By using GDEs in $CO_2$RR, researchers have achieved high current densities exceeding 100 mA $cm^2$, which are an order of magnitude greater than that obtained with traditional aqueous systems under similar conditions.[76,77]

In recent advancements in $CO_2$RR technologies, GDEs and membrane electrode assemblies (MEAs) have been pivotal in achieving higher performances.[78,79] GDEs are assembled into MEAs by first depositing a catalyst layer onto a porous gas diffusion layer (GDL), and then hot-pressing this assembly onto a pre-treated proton exchange membrane (PEM) to ensure proper adhesion and optimal contact. Subsequently, this integrated structure is incorporated into the electrochemical cell, facilitating efficient gas transport, catalyst utilization, ion conductivity for enhanced $CO_2$ reduction performance, and efficient removal of products. This design is beneficial to maintain an optimal chemical environment at the catalyst surface, which is crucial for enhancing the $CO_2$RR rate and selectivity. The use of GDEs is particularly effective in

 This journal is © The Royal Society of Chemistry 2024

Published on 25 August 2024. Downloaded on 02.05.26 08:00:32.

suppressing HER by ensuring a higher local concentration of $CO_2$ and reducing the $CO_2$ diffusion distance.[80–82] MEA cells incorporating GDEs have demonstrated significant potential in scaling up $CO_2$RR for industrial applications.[83] For instance, the highest reported current densities and faradaic efficiencies (FE) in $CO_2$RR to date have been achieved in flow cells utilizing GDEs.[84–87]

## 2. MOFs for electrochemical $CO_2$ reduction

One of the first examples of the application of MOF in $CO_2$RR was reported by Kumar *et al.*[88] in 2012, where they studied the catalytic performance of $Cu_3(BTC)_2$ immobilized on glassy carbon (GC) in a non-aqueous medium (DMF, comprising tetrabutylammonium tetrafluoroborate, as the supporting electrolyte, saturated with $CO_2$). Oxalic acid (the product) was detected with a faradaic efficiency (FE) of 51%. The highly reproducible reversible redox reactions of Cu(II)/Cu(I) and Cu(I)/Cu(0) were revealed by cyclic voltammetry (CV) measurements in a KCl solution of 0.1 M, indicating the mechanical and electrochemical stability of MOF film@GCE under the experimental conditions. These redox peaks were not observed in copper foil or electrochemically deposited copper metal. In the same year, Hinogami *et al.*[89] described a copper rubeanate metal–organic framework (CR-MOF) coated on carbon paper (CP) as the working electrode for $CO_2$RR in 0.5 M $KHCO_3$ aqueous solution. Cyclic voltammetry revealed that this CR-MOF was more active compared to the Cu electrode, with a selectivity of more than 98% towards the formation of HCOOH. The remaining was attributed to hydrogen selectivity. However, the Cu electrode produced a range of products, including HCOOH, CO, and hydrocarbons. This variation in product selectivity obtained by CR-MOF and metallic Cu was assigned to the different electronic environments of Cu in the two structures, where in CR-MOF, Cu is coordinated to organic ligands, and thus it is ionic and the density of electrons is lower than that in metallic Cu. The decreased electron density resulted in weak $CO_2$ adsorption on the reaction site on CR-MOF, leading to the preferential formation of HCOOH. Achieving different products in these two studies over Cu-based MOFs as electrocatalysts can be explained as follows: Kumar *et al.*[88] applied 1,3,5-benzenetricarboxylic acid (BTC) as the ligand, which contains oxygen atoms (hard donors) coordinated to Cu, while in CR-MOF, the ligand contains N and S donor atoms (soft donors), resulting in the formation of a different electronic environment of metal ions, and accordingly different catalytic activity. Furthermore, the reaction medium in these two studies was different, where in the research performed by Kumar *et al.*, the electrolyte was organic (less protons) compared to the work carried out by Hinogami *et al.*,[89] where an aqueous solution (abundant protons) was employed. Alternatively, Kang *et al.*[90] investigated the effect of different types of ionic liquids (IL) as electrolytes on the product of electrochemical reduction of $CO_2$ over Zn-1,3,5-benzene tricarboxylic acid metal–organic frameworks (Zn-BTC MOFs). The morphology of Zn-MOFs significantly influenced the electrochemical reduction of $CO_2$, with sheet-like Zn-MOFs displaying the greatest activity due to their expansive electroactive surface areas. The effectiveness of the electrolytes is enhanced by using imidazolium-based ILs with fluorine, which interact more strongly with $CO_2$, leading to a higher performance. This combination resulted in a $CH_4$ selectivity exceeding 80% under the optimal conditions, demonstrating the critical role of both the MOF structure and composition of the ILs in the reaction efficiency.

### 2.1 Selectivity

At this stage, the low selectivity for $CO_2$RR has been a challenge that is worth considering. When an aqueous electrolyte is employed in $CO_2$RR, HER is a competitive process due to its lower kinetic barrier in comparison to $CO_2$RR. In addition, unlike HER, which is a single-product reaction, in $CO_2$RR, different carbon-based products, including CO, formate, alcohols, and hydrocarbons may be produced. In this case, multiple MOFs have been created with different metal centers and organic linkers to be applied in $CO_2$RR to produce CO, alcohols, hydrocarbons, or formate with high selectivity. Electrochemical $CO_2$RR is a sustainable pathway to produce syngas, where a stream of CO can be generated from $CO_2$, $H_2O$, and electricity at a high yield under near ambient conditions. Given that CO is a more valuable syngas product,[91] efforts have been devoted to driving the $CO_2$RR to the highest possible selectivity for CO.[92] In this aspect, several MOFs have been applied in $CO_2$RR to produce CO as the significant product, including ZIF-based catalysts,[93–95] 1,10-phenanthroline-doped ZIF-8,[96] porphyrin-based MOFs,[45,47,97–100] nanoparticles embedded in porphyrin-based MOFs,[101] and phthalocyanine-based MOFs.[102,103]

In an interesting example, Hod *et al.*[97] developed a catalyst with an FE of almost 100% *via* the deposition of MOF-525, which contained *meso*-tetra(4-carboxyphenyl)porphyrin ($H_4$TCPP) as a linker and Zr as the metal node on glass substrates doped with tin oxide fluoride (FTO), followed by post-treatment of the MOF thin film with iron chloride to metalate $H_4$TCPP by iron (Fig. 5a). Three distinct redox waves attributed to Fe(III/II) ($E_f = -0.32$ V *vs.* NHE), Fe(II/I) ($E_f = -0.87$ V *vs.* NHE), and Fe(I/0) ($E_f = -1.4$ V *vs.* NHE) were observed in the CV measurements, signifying the charge transfer by redox hopping between the Fe-TCPP adjacent sites enabled by the Fe-MOF-525 film (Fig. 5b). CO (15.3 μmol $cm^{-2}$) and $H_2$ (14.9 μmol $cm^{-2}$) were determined to be the main products. It was demonstrated that the addition of 1 M 2,2,2-trifluoroethanol (TFE) to the catalytic reaction as a weak Brønsted acid resulted in an increase in current density to 5.9 mA $cm^{-2}$ (Fig. 5c), and also higher catalyst stability, which is in accordance with the results obtained for the homogeneous catalyst (Fe-TPP) by adding TFE.[105] Achieving high selectivity toward formate in the electrolysis process is energetically inefficient and is attainable at high cathodic potentials. Interestingly, among the various materials applied in the production of formate *via* $CO_2$ electrolysis, MOF-based catalysts show potential as excellent platforms for determining the design characteristics of electrocatalysts[106] and bimetallic catalysts.[107] This can be

Published on 25 August 2024. Downloaded on 02.05.26 08:00:32.

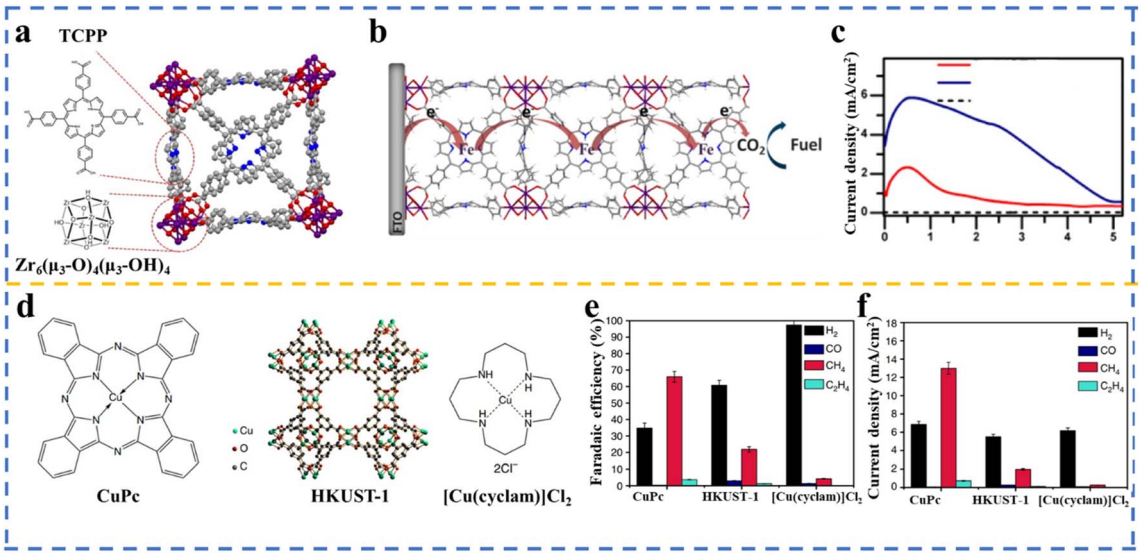


Fig. 5 (a) Illustration of a part of MOF-525 and the structure of the TCPP ligand and the $Zr_6$-based node. (b) Transfer charge by redox hopping between neighboring Fe-TCPP sites. (c) Current density of Fe-MOF-525 obtained under various conditions. Reproduced with permission.[97] Copyright 2015, the American Chemical Society. (d) Structure of HKUST-1 (copper(II) benzene-1,3,5-tricarboxylate (BTC) MOF), copper(II) phthalocyanine (CuPc), and copper(II) 1,4,8,11-tetraazacyclotetradecane chloride [Cu(cyclam)]$Cl_2$. (e) Faradaic efficiency (%) and (f) current density over three Cu-based catalysts at −1.06 V *vs.* RHE. Adopted with permission.[104] Copyright 2018, Nature Publishing Group.

ascribed to the molecular nature of MOFs and their well-defined tunable structure, enabling detailed studies of the reaction mechanism and reactive intermediates. $CO_2$-derived methane could be effectively utilized in energy infrastructure. To realize the production of potential solar fuel,[9,108] MOFs can be promising candidates to convert $CO_2$ to hydrocarbons in electrocatalysis reactions.[104,109] In the research carried out by Weng *et al.*,[104] the electrocatalytic activity of the HKUST-1 MOF (comprised of copper(II) and benzene-1,3,5-tricarboxylate (BTC)) together with copper(II) 1,4,8,11-tetraazacyclotetradecane chloride ([Cu(cyclam)]$Cl_2$) and copper(II) phthalocyanine (CuPc) towards $CH_4$ production was investigated, in which Cu(II) was located in a different electronic structure (Fig. 5d). The CuPc catalyst exhibited the highest activity (FE of 66%) and selectivity to produce $CH_4$ compared to [Cu(cyclam)]$Cl_2$ and HKUST-1 (Fig. 5e and f, respectively). Alcohols, including methanol and ethanol, are other targets that can be produced *via* the electrochemical reduction of $CO_2$. Thus, methanol will be directly produced without applying fossil fuels, and interestingly the synthesized methanol can be converted to gasoline.[110] In the discussion of applied materials in $CO_2$RR to produce alcohols, Cu is one of the most promising transition metals applied in $CO_2$ reduction to obtain alcohol and hydrocarbons; nonetheless, the achieved selectivity of the products is low.[111] In this regard, several Cu-based MOFs have been successfully utilized in $CO_2$RR to produce alcohols.[112–114] In a study performed by Perfecto-Irigaray *et al.*,[115] a faradaic efficiency of 47.2% associated with methanol and ethanol was achieved over a Cu-based MOF. They applied doped metals, including Ru(III), Zn(II), and Pd(II), to partially replace the Cu(II) atoms in the structure of HKUST-1. It was demonstrated that the Ru-doped samples had a noticeable positive impact on the alcohol yield, while Pd(II) hindered the electroreduction of $CO_2$ to liquid products. In a recent study, Zhang *et al.* demonstrating that manipulating the coordination environment of copper as the metal active site in a copper-based metal–organic framework (Cu-MOF) with various halogen atoms resulted in an improved selectivity for $CH_4$ production in the $CO_2$ reduction reaction ($CO_2$RR).[116] A list of the MOFs employed in the $CO_2$RR to produce a range of products is presented in Table 2.

### 2.2 Role of MOFs in tuning the micro-environment during $CO_2$RR

Compared with conventional catalysts, MOFs are unique in that they are comprised of three distinct sites for catalytic functions, *i.e.*, a metal component, organic linker, and pore space. This structure provides ordered architectures and customizable chemical functionalities, which are advantageous for establishing accurate structure–activity relationships for $CO_2$RR. This highlights the potential utility of MOFs, offering a fundamental understanding of how different structural features at the molecular level contribute to selectivity and catalytic efficiency. Recent studies have demonstrated the substantial modular tunability of $CO_2$RR activity and selectivity by carefully tailoring the coordination microenvironment of the metal centres within MOF structures.[121] For instance, Meng and colleagues achieved tunable control of the catalytic performance by precisely modulating the chemical and structural features at the atomic level. They used four structural analogues of conductive two-dimensional (2D) MOFs made of metallophthalocyanine (MPc) ligands linked by Cu nodes. The catalytic performance, including activity and selectivity, was found to be governed by two key structural factors, *i.e.*, the metal within the MPc (Co *vs.* Ni) catalytic subunit and the identity of the heteroatomic cross-

 This journal is © The Royal Society of Chemistry 2024

Published on 25 August 2024. Downloaded on 02.05.26 08:00:32.

Table 2 Electrocatalytic reduction of $CO_2$ catalyzed by metal–organic frameworks

| Electrocatalyst | Applied potential | Electrolyte | Active site | Catalytic efficiency (%) | Ref. |
|---|---|---|---|---|---|
| NNU-15 | −0.6 V *vs.* RHE[a] | 0.5 M $KHCO_3$ | Ligand (TIPP) | $FE_{CO} = 99.2$ | 45 |
| Co porphyrin[b] MOF($Al_2(OH)_2$TCPP-Co) | −0.7 V *vs.* RHE | 0.5 M $K_2CO_3$ | Ligand (Co-TCPP) | $FE_{CO} = 76$ | 47 |
| Cu-based MOF | −2.5 V *vs.* Ag/AgCl | 0.01 M TBATFB/DMF[c] | Metal cluster (Cu–O) | $FE_{oxalate} = 51$ | 88 |
| Copper rubeanate MOF | −1.2 V *vs.* SHE[d] | 0.5 M $KHCO_3$ | Metal cluster (Cu–O) | $FE_{HCOOH} = 42$ | 89 |
| Zn-BTC MOFs | −2.2 V *vs.* $Ag/Ag^+$ | [e]$BmimClO_4$ | Metal cluster (Zn–O) | $FE_{CH_4} = 88.3$ | 90 |
| ZIF-8 | −1.8 V *vs.* SCE[f] | 0.5 M NaCl | Metal node (Zn–O) | $FE_{CO} = 65$ | 93 |
| ZIF-8 | −1.1 V *vs.* RHE | 0.25 M $K_2SO_4$ | Metal cluster (Zn–O) | $FE_{CO} = 81$ | 94 |
| $Ni(Im)_2$ nanosheets | −0.85 V *vs.* RHE | 0.5 M $KHCO_3$ | Metal nodes ($Ni^{2+}$) | $FE_{CO} = 78.8$ | 95 |
| 1,10-Phenenthroline doped ZIF | −1.1 V *vs.* RHE | 0.1 M $KHCO_3$ | Ligand(2-methylimidazole) and 1,10-phenanthroline | $FE_{CO} = 90.6$ | 96 |
| MOF-525 | −1.3 V *vs.* NHE | [g]1 M $TBAPF_6$ | Ligand (Fe-TCPP) | $FE_{CO}$ = almost 55 | 97 |
| TCPP(Co)/Zr-BTB-PSABA[h] | −0.769 V *vs.* RHE | 0.5 M $KHCO_3$ | Co | $FE_{CO} = 85.1$ | 98 |
| PCN-222(Fe) | −0.6 V *vs.* RHE | 0.5 M $KHCO_3$ | Ligand (Fe-TCPP) | $FE_{CO} = 91$ | 99 |
| Co-PMOF[i] | −0.8 V *vs.* RHE | 0.5 M $KHCO_3$ | Metal cluster (Zn-ε-Keggin cluster) | $FE_{CO} = 98.7$ | 100 |
| Ag@Al-PMOF[j] | −1.1 V *vs.* RHE | 0.1 M $KHCO_3$ | Metal (Ag) | $FE_{CO} = 55.8$ | 101 |
| MOF-1992 | −0.52 V *vs.* RHE | 0.1 M $KHCO_3$ | Ligand (CoPc) | $FE_{CO} = 80$ | 102 |
| PcCu–$O_8$–Zn | −0.7 V *vs.* RHE | 0.1 M $KHCO_3$ | Metal cluster ($ZnO_4$) | $FE_{CO} = 88$ | 103 |
| GDE[k]-Cu(BTC) | −2.3 to −2.5 V *vs.* SCE | 0.5 M $NaHCO_3$ | Metal cluster (Cu–O) | $FE_{CH_4} = 11$ | 109 |
| HKUST-1doped Zn(II), Ru(III) and Pd(II) | CP[l] mA $cm^{-2}$ | 0.5 M $KHCO_3$ | Ru(III) | $FE_{CH_3OH \text{ and } C_2H_5OH} = 47.2$ | 112 |
| Cu and Bi-based MOF (HKUST-1/CAU-17 blends) | −0.1 to −0.7 V *vs.* RHE | 0.5 M $KHCO_3$ | (CAU-17) | $FE_{CH_3OH} = 8.6$, $FE_{C_2H_5OH} = 28.3$ | 113 |
| HKUST-1 | −1.16 V *vs.* Ag/AgCl | 0.5 M $KHCO_3$ | Metal cluster (Cu–O) | $FE_{CH_3OH} = 5.6$, $FE_{C_2H_5OH} = 10.3$ | 114 |
| Cu-MOF with Cu–Cl, –Br, –I coordination | −1.08 *vs.* RHE | 1 M KOH | Cu–halogen | $FE_{CH_4} = 57.2$ for Cu–I | 116 |
| Cu nanoparticles@NU1000 | −0.82 V *vs.* RHE | 0.1 M $NaClO_4$ | Metal (Cu) | $FE_{formate} = 31$ | 117 |
| ReL[m]$(CO)_3Cl$ | −1.6 V *vs.* NHE[n] | 0.1 M TBAH[o]/MeCN | Ligand[p] (ReI$(CO)_3$ (dcbpy) Cl) | $FE_{CO} = 93$ | 118 |
| HKUST-1 | −1.06 V *vs.* RHE | 0.5 M $KHCO_3$ | Metallic Cu nanoclusters | $FE_{CH_4} = 27$ | 119 |
| ZIF-8 doped with Fe, Ni, Cu | −1.0 *vs.* RHE | 0.5 M $KHCO_3$ | Imidazolate ligand | $FE_{CO} = 88.5$ | 120 |

[a] Reversible hydrogen electrode. [b] TCPP-$H_2$ = 4,4′,4″,4‴-(porphyrin-5,10,15,20-tetrayl)tetrabenzoate. [c] Tetrabutylammonium tetrafluoroborate/dimethylformamide. [d] Standard hydrogen electrode. [e] 1-Butyl-3-methylimidazolium perchlorate. [f] Saturated calomel reference electrode. [g] Tetrabutylammonium hexafluorophosphate. [h] *p*-Sulfamidobenzoic acid. [i] Polyoxometalatemetalloporphyrin organic frameworks. [j] Al-PMOF [$Al_2(OH)_2$(TCPP)], TCPP = tetrakis(4-carboxyphenyl)porphyrin. [k] Gas diffusion electrode. [l] Chronopotentiometry. [m] L = 2,2′-bipyridine-5,5′-dicarboxylic acid. [n] Normal hydrogen electrode. [o] Tetrabutylammonium hydroxide. [p] 4,4′-Dicarboxylic-2,2′-bipyridine.

linkers (O *vs.* NH) between these subunits. Among the MOFs, CoPc–Cu–O showed the highest selectivity toward CO with an FE of 85% and high current densities of up to −17.3 mA $cm^{-2}$ at a low overpotential of −0.63 V. The mechanistic studies supported by DFT calculations indicated that the CoPc-based and O-linked MOFs have lower activation energies for the formation of carboxyl intermediates, resulting in higher activity and selectivity compared to their NiPc-based and NH-linked analogues. These findings present a novel approach for designing high-performance $CO_2$ reduction catalysts by strategically combining various structural factors, such as active metal sites, peripheral groups, and secondary sites.[122]

It was also observed that a catalyst featuring dual-copper sites anchored on ultrathin boron imidazolate layers (BIF-102NSs) could significantly enhance the FE and selectivity for $C_2H_4$ production. The catalyst design leveraged the modular tunability of MOFs, allowing precise control of the local chemical environment around the active sites. The dual-copper sites within the MOF structure were found to create a cooperative interaction, which enhanced the adsorption and activation of $CO_2$ molecules. The $Cl^-$ ions bridging the $Cu_2$ units in BIF-102NSs played a crucial role in modulating the electronic states and adsorption energies, facilitating the C–C coupling necessary for the formation of multi-carbon products. Electrocatalytic tests showed that BIF-102NSs achieved an FE of 11.3% for $C_2H_4$ production, which was significantly higher than its isoreticular counterpart BIF-103 (7.15%) and single-metal counterpart BIF-104 (3.55%). The enhanced performance was

Published on 25 August 2024. Downloaded on 02.05.26 08:00:32.

attributed to the cooperative nature of the dual-metal sites, which resulted in charge enrichment at the surrounding Cu centres. This charge enrichment is crucial for stabilizing the reaction intermediates and lowering the activation energy barriers, highlighting the importance of the local micro-environment in determining the $CO_2$RR outcomes.[123] Likewise, Cu-HITP (HITP = 2,3,6,7,10,11-hexaiminotriphenylene), a 2D MOF featuring $CuN_4$ nodes, effectively stabilized the key intermediates for C–C coupling. *In situ* infrared spectroscopy and DFT calculations demonstrated that a polydopamine (PDA) coating on Cu-HITP creates a $CO_2$ reduction-favourable local environment, enriched with proton sources and hydrogen-bond donors around the bi-copper active sites. This combination promoted *CO hydrogenation and stabilized the crucial intermediates (*COH and *OCCOH), leading to high selectivity for $C_{2+}$ reduced products, achieving FEs of 75% for $C_{2+}$ products and 51% for $C_2H_4$ in $KHCO_3$ electrolyte.[124]

Sun and co-workers developed a series of $Cu_4X$ cluster-based MOFs ($[Cu_4X(TIPE)_3]\cdot 3X$, [X = Cl, Br, I], TIPE = 1,1,2,2-tetrakis(4-(imidazole-1-yl)phenyl)ethene) to investigate the influence of different halogen atoms in the nodes on the selectivity of $CO_2$RR products. The results showed that the Cu–I MOF achieved the highest FE for $CO_2$RR of up to 83.2% at −1.08 V *vs.* RHE and a current density of 88 mA $cm^{-2}$. The FE for $CH_4$ ($FE_{CH_4}$) was above 50% over a wide potential range, with a maximum $FE_{CH_4}$ of 57.2% at −1.08 V and a partial current density of 60.7 mA $cm^{-2}$. In comparison, the highest $FE_{CH_4}$ for Cu–Cl and Cu–Br was only 32.9% and 40.2% at −1.28 V, respectively. The improved performance of the Cu–I MOF was attributed to the larger radius of the iodine atom, which modulated the electronic properties of the Cu active sites. DFT calculations indicated that the formation energy of the intermediates in the potential-determining steps decreased with an increase in the radius of the halogen atom, explaining the superior catalytic activity of the Cu–I MOF for $CO_2$-to-$CH_4$ conversion. The halogen atoms in the $Cu_4X$ clusters altered the d-band centre of the Cu atoms, facilitating the adsorption and activation of $CO_2$ molecules and improving the C–C coupling process, which is crucial for producing multi-carbon products like $CH_4$.[125]

A nitrile-modified MOF (UiO-66-CN) assembled on the surface of Bi-foil significantly enhanced the local concentration of $CO_2$ near the catalyst surface, increasing it by approximately 27 times compared to the bulk electrolyte, reaching 0.82 M. This concentration boost was crucial for improving the $CO_2$RR reaction rate, given the typically low solubility of $CO_2$ in aqueous solutions. Additionally, the MOF stabilized the reaction intermediates, as revealed by *operando* infrared spectroscopy and supported by DFT simulations, effectively lowering the energy barriers for their conversion into HCOOH. This stabilization fine-tuned the reaction pathways, enhancing both the selectivity and efficiency of $CO_2$RR. By increasing the local $CO_2$ concentration and stabilizing the reaction intermediates, the MOF also reduced the competition from the HER, allowing $CO_2$RR to proceed more selectively and efficiently. In a conventional H-cell setup, the catalyst achieved a faradaic efficiency of up to 93% for HCOOH, with seven times faster kinetics at −0.75 V *vs.* RHE. When used in the GDE configuration, the current density for HCOOH production reached levels suitable for technical applications at 166 mA $cm^{-2}$.[126]

### 2.3 MOF stability in $CO_2$RR

Some MOFs can encounter stability challenges due to their relatively weak metal coordination bonds, which make them susceptible to water. In the presence of water, hydrolysis of these metal-linker bonds may occur, leading to the irreversible degradation of the MOF framework and the formation of metal hydroxides or hydrated metal species. This potential instability in water, as well as acidic or basic environments, can limit their practical applications in electrocatalysis, particularly under aqueous conditions.[127] The stability of MOFs is influenced by the properties of their linker and inorganic cluster, where higher p$K_a$ coordination sites and hydrophobic ligands can enhance their stability by forming stronger bonds and protecting their metal centers.[128,129] To address the above-mentioned challenges, researchers are focusing on understanding and improving the stability of MOFs under various conditions. This includes exploring the alkalinity of organic ligands, strengthening metal coordination bonds, and shielding functional groups. Stability considerations also extend to the attachment of MOFs to electrode surfaces and their structural integrity under the reaction conditions. Ensuring strong chemical bonding between the MOF and the electrode surface is crucial for long-term stability, with direct growth of MOFs on the electrode forming robust films that prevent their detachment. However, their structural stability can still be compromised by interactions with the electrolyte, reaction intermediates, or applied current, making the metal–ligand bonds particularly vulnerable to hydrolysis.

Under aqueous conditions, MOFs built from high-valence metals such as $Zr^{4+}$ and $Ti^{4+}$ with carboxylate ligands often show good stability in aqueous media, although they may be unstable at certain pH levels.[130] Low-valent metal MOFs with azolate ligands tend to hydrolyse under acidic conditions, while high-valent metal MOFs with carboxylate ligands can decompose in alkaline media.[131] Certain anions in solution, such as hydroxide, carbonate, and phosphate, can also destabilize MOFs by competing with their carboxylate ligands for metal coordination. This issue becomes especially concerning during $CO_2$RR, given that it is commonly conducted in aqueous neutral electrolytes, such as $CO_2$-saturated bicarbonate and phosphate buffer, which can exacerbate the instability of MOFs.[132]

There are numerous reports on MOFs demonstrating stability in $CO_2$RR across both aqueous and non-aqueous electrolytes. These MOFs are capable of producing a range of products, from simple 2-electron reduction products such as CO and formic acid to more complex products such as ethylene and acetic acid, showcasing their versatility and robustness under various reaction conditions.[94,95,133–142] However, some studies have demonstrated that MOFs can undergo structural evolution during the catalytic process, leading to their potential deactivation, loss of their surface area, or the formation of new active phases. For example, Yang *et al.* reported the formation of

 This journal is © The Royal Society of Chemistry 2024

Published on 25 August 2024. Downloaded on 02.05.26 08:00:32.

Cu nanoparticles functionalized by nitrogen-containing ligands during $CO_2$ electrolysis on a Cu–adenine MOF. This transformation was crucial to the high efficiency of $CO_2$ conversion into hydrocarbons, achieving FEs of over 73% for hydrocarbons, with notable selectivity for ethylene and methane.[143] Similarly, the HKUST-1 MOF underwent structural decomposition during $CO_2$RR, leading to the formation of Cu clusters, which act as active sites for catalysis. This structural evolution was confirmed through *in situ* XAS and EPR studies.[144] In the case of CuHHTP MOF (HHTP = hexahydroxytriphenylene), its decomposition during $CO_2$RR resulted in the formation of $Cu_2O$ quantum dots. These quantum dots served as highly active catalytic sites, demonstrating a significant FE of 73% for the production of $CH_4$.[145] These examples underscore the importance of thorough material characterization before and after the catalytic process to identify the active species and understand the structural evolution of MOFs under the reaction conditions.

Given the potential for pristine MOFs to decompose during $CO_2$RR, rigorous characterization techniques are essential to confirm their stability. In the case of MOF decomposition during electrocatalysis, it will be crucial to confirm that the observed carbon products originate from $CO_2$ rather than from the decomposition of the MOF structure during electrocatalysis. Several characterization techniques can be used to either prove the stability or demonstrate the decomposition of MOFs under the operation conditions. For this purpose, both post-catalysis and *in situ*/*operando* characterization methods can be employed to ensure their structure stability and the source of the reduction products. Post-catalysis characterization techniques such as XRD, TEM, and XPS are crucial for analyzing the structural and compositional changes in MOFs after $CO_2$RR. XRD can identify any loss of crystallinity or the emergence of new structures/phases within the MOF material, while TEM can visualize the formation of metal nanoparticles or other decomposition products. XPS can offer detailed information about changes in the chemical states and bonding environments of the metal centers, providing further evidence of whether the MOF has maintained its structural integrity. *In situ*/*operando* spectroscopic techniques, such as *in situ* ATR-FTIR, Raman spectroscopy, and XAS (involving extended X-ray absorption fine structure [EXAFS] and X-ray absorption near edge structure [XANES]) provide real-time insight into the structural integrity of MOFs during the $CO_2$RR process. These techniques can monitor the changes in the metal oxidation states, the formation of the reaction intermediates, and any structural transformations within the MOF. By continuously tracking these parameters, researchers can detect whether the MOF remains intact or begins to decompose under the electrochemical conditions, thereby identifying the actual active species involved in the catalytic process. Isotope labeling with $^{13}CO_2$ is also one of the most effective techniques to directly trace the carbon atoms involved in the reaction. Using $^{13}CO_2$ as a feedstock allows tracking of the carbon atoms in the resulting products, thereby confirming whether they originate from $CO_2$ or the MOF framework. This approach, often combined with mass spectrometry or NMR spectroscopy, offers a robust way to validate the source of the carbon in the reaction products, ensuring that the observed products are genuinely the result of $CO_2$ reduction.[146–150]

### 2.4 Limitations of pristine MOF-based electrocatalysts

Although MOF materials have an ideal porous structure for $CO_2$ adsorption, they face several drawbacks that hinder their commercial/industrial application in $CO_2$RR. In addition to their low hydrolytic stability over a wide range of pH, as discussed in the previous section,[151] the poor electrical conductivity of many MOFs leads to a low charge transfer efficiency, resulting in significant ohmic losses during catalysis. This electrically insulating nature of bulk MOFs affects the overall charge transport rate within the framework. Furthermore, the lack of mesoporosity in MOF materials is a limitation given that mesoporosity facilitates liquid mass transfer.[47] Given these limitations, researchers were propelled to convert MOFs into more durable and long-lasting materials. Interestingly, inorganic nanomaterials (metal sulfides[151] or metal oxides[152,153]) and organic–inorganic hybrid nanomaterials (carbon composites[154,155]) can be fabricated *via* the electrochemical or thermal treatment of MOFs in the air or inert atmosphere. These materials demonstrate higher stability, and in the case of carbon-based MOFs, higher conductivity compared to their parent MOFs. In addition, the inherent properties of the parent MOFs, such as porosity features and high surface areas. Therefore, the use of MOF-derived materials for $CO_2$ electrochemical reduction has attracted growing attention, which is the crucial point of this study and will be discussed further in the following sections.

## 3. MOF-derived composites for electrochemical $CO_2$RR

Carbon-based nanoporous materials are attractive catalysts in electrochemical reactions due to their chemical stability, high electrical conductivity, and the presence of a significant number of mesopores, which can improve the mass transfer of the liquid phase.[156–158] As alternatives to metals such as Ag and Au-based catalysts in electrocatalysis,[159,160] carbon-supported transition metal catalysts doped with nitrogen (denoted as NC) display unique electrical and chemical characteristics. Moreover, these materials are less susceptible to poisoning, making them more robust in catalytic applications.[161] Interestingly, the arrangement of transition metals within the carbon framework significantly influences the product selectivity and catalytic activity. For instance, when iron atoms are bonded with heteroatoms such as nitrogen and/or oxygen in a carbon matrix, the reaction tends to produce CO.[162] In contrast, iron nanoparticles anchored to a nitrogen-doped carbon (NC) support primarily lead to the generation of $H_2$.[163]

Regarding this matter, the unique characteristics of MOFs offer a promising approach to providing well-dispersed active sites throughout their networks. This highlights the fact that MOFs are excellent catalyst precursors for creating hybrid catalysts incorporating metal (oxides) nanoparticles and porous carbon materials.[164] The resulting product inherits the porous

Published on 25 August 2024. Downloaded on 02.05.26 08:00:32.

structure from its parent MOF and has the stability required in $CO_2$RR. Moreover, there is a possibility to introduce a variety of heteroatoms, including N, S, and P, into the MOF-derived carbon structure by choosing diverse organic linkers and modulators. In this case, the properties of the catalyst, such as chemical, electrical and functional characteristics, can be tuned.[165]

Among the carbon-based electrocatalytic materials produced *via* MOF templates, zeolitic imidazolate framework (ZIF)-derived carbons are considerably investigated, specifically those originating from ZIF-8. This group of MOFs has attracted attention in $CO_2$RR due to their high surface area, microporous structures, facile synthesis, and presence of nitrogen atoms in the imidazolate linker (given that it creates the possibility to distribute the heteroatom N in the carbon matrix after carbonization). Moreover, during the carbonization process, zinc (the metal node in ZIF-8) will evaporate from the final carbon structure because of the high temperature and there is the possibility to subsequently incorporate active metal sites through various approaches; this strategy has been applied for the design of catalytic materials dedicated to electrochemical $CO_2$RR, as addressed in the following section.

### 3.1 Supported MOF-based materials

The pyrolysis of multiwall carbon nanotube (MWCNT)-supported Fe-ZIF-8 promoted the generation of N-doped porous carbon (NPC) (ZIF-CNT-FA) (Fig. 6a and b), which exhibited an FE of almost 100% towards CO production and a current density up to 7.7 mA $cm^{-2}$ at an overpotential of 740 mV.[166] It was concluded that the efficient mass and electron transport provided by the CNT support and the significant content of Fe–$N_x$ and pyridinic-N as active sites enhanced the catalytic performance. The superior selectivity for CO was achieved through MWCNT, which accelerated the electron and $CO_2$ transport. Moreover, Huang and coworkers[48] employed an oxygen-rich MOF (Zn-MOF-74) to prepare N-doped porous carbon (NPC) (Fig. 6c), which featured a high percentage of active nitrogen (pyridinic and graphitic N) sites and possessed a highly porous structure. Through the optimization of the calcination time and temperature, the amount of the active N species could be regulated. The resultant electrocatalyst was efficient for $CO_2$RR with a high CO FE of 98.4% at −0.55 V *vs.* RHE (Fig. 6d and e).

Embedding nanoparticles in MOF-based materials is another reliable means of obtaining an efficient $CO_2$RR electrocatalyst. MOF-derived NPC-doped Bi nanoparticles (Bi@NPC) (Fig. 6f) with a unique microstructure achieved a higher $CO_2$ adsorption capacity and faster electrochemical $CO_2$ reduction to formate than the conventional Bi nanoparticles (Fig. 6g).[167] At the low potential of 1.5 V (*vs.* SCE) in 0.1 M $KHCO_3$ solution, Bi@NPC demonstrated a high formate selectivity of 92.0% and excellent formate current density of

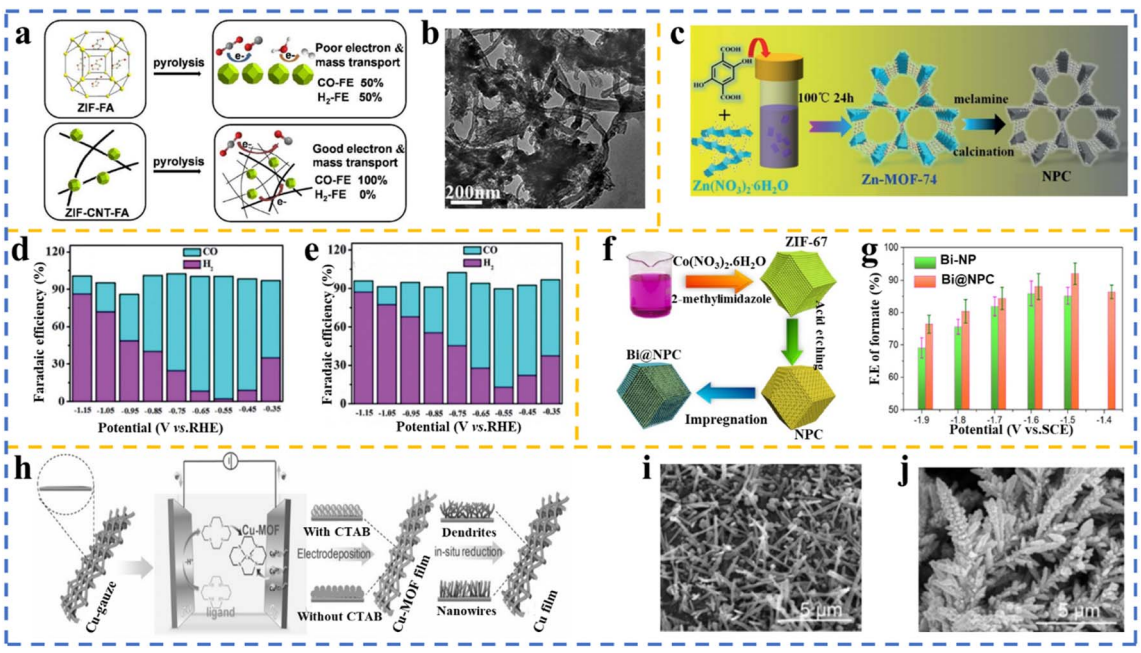


Fig. 6 (a) Schematic of enhanced CO FE obtained over MWCN-supported pyrolyzed ZIF for the $CO_2$RR as a result of enhanced electron conductivity and mass transport in these catalysts compared to pyrolyzed ZIF-FA. (b) TEM image of the MWCN-supported pyrolyzed ZIF catalysts. Reproduced with permission.[166] Copyright 2017, the Royal Society of Chemistry. (c) Schematic representation of the synthesis of nitrogen-doped porous carbon (NPC) derived from Zn-MOF-74. (d and e) Faradaic efficiency obtained over NPC and porous carbon (PC), respectively. Reproduced with permission.[48] Copyright 2020, Wiley-VCH. (f) Schematic demonstrating the approach of embedding Bi nanoparticles in MOF-derived nitrogen-doped porous carbon Bi@NPC and (g) comparison of faradaic efficiency obtained over Bi-NP and Bi@NPC. Reproduced with permission.[167] Copyright 2020, Elsevier. (h) Illustration of the preparation process for the Cu-MOF film and its derivatives on Cu-gauze. (i) SEM image of Cu-MOF-1 derivative formed on Cu-gauze at electrodeposition without CTAB. (j) SEM image of the Cu-MOF-1 derivative formed on Cu-gauze *via* electrodeposition with CTAB, Reproduced with permission.[168] Copyright 2020, Wiley-VCH.

 This journal is © The Royal Society of Chemistry 2024

Published on 25 August 2024. Downloaded on 02.05.26 08:00:32.

14.4 mA $cm^{-2}$. On continuous electrolysis, Bi@NPC showed no significant degradation over 12 h.

A potential method to take advantage of the intrinsic and distinguishing characteristics of MOF-derived materials as thin films is the direct growth of active materials on three-dimensional (3D) porous conductive substrates. This technique can enhance the active catalytic sites and rates[169–171] due to the enhanced mass transport capacity and the diminished contact resistance, which will lead to smooth electron transfer. Therefore, hollow Cu-MOF thin films were developed on 3D Cu gauze (Cu-G) through a facile and controllable strategy, as reported by Zhu *et al.*[168] By applying an electrochemically assisted self-assembly technique, hollow Cu-MOF was formed on the anode (Cu-gauze substrate), which acted as a source of copper ions in an electrolyte of ethanol/water containing surfactant as a structure-directing agent. During the reduction of $CO_2$, the dendritic $Cu^0$ was realized because of the reduction of the hollow Cu-MOF. At the same time, Cu-MOF (the MOF formed without using surfactant) resulted in the formation of $Cu^0$ nanowires (Fig. 6h–j). Linear sweep voltammetry (LSV) was carried out to assess the catalytic activity of the electrocatalysts, employing $CO_2$-saturated 1-butyl-3-methylimidazolium tetrafluoroborate ($BmimBF_4$, 0.5 M)/acetonitrile (MeCN)/$H_2O$ (1.0 M) electrolyte. At −1.85 V *versus* $Ag/Ag^+$, the highest current density and FE (102.1 mA $cm^{-2}$ and 98.2%, respectively) were obtained over dendritic $Cu^0$ in comparison to $Cu^0$ nanowires, Cu NPs, and $Cu_2O$. In addition, the electrochemical active surface area (ECSA) analysis revealed that the dendritic $Cu^0$ sample had the largest ECSA compared to $Cu^0$ nanowires, Cu NPs, and $Cu_2O$. Interestingly, it was demonstrated that the generation of formate was a potential function, given that both FE and current density for formate increased quickly with an increase in the negative potential and at −1.85 V *vs.* $Ag/Ag^+$, reached the maximum of 98.2% before dropping. Furthermore, it was indicated that the FE and the current density of formate were higher in IL/MeCN/$H_2O$ than in the aqueous electrolyte at all the applied potentials.

### 3.2 MOF-derived single-atom/site catalysts

Different methods such as metal oxidation, sulfiding, phosphiding, and metal alloying have been demonstrated to successfully engineer transition metal (TM) electronic states for improved $CO_2$RR activities. However, these processes often result in complex atomic structures and coordination, complicating the study and understanding of the possible catalytic active sites. Alternatively, introducing TM atoms in a well-established material matrix can create significant opportunities to tune the electronic properties of TMs as $CO_2$RR active sites, while maintaining a relatively simple atomic coordination for fundamental mechanism studies. Moreover, TM atoms trapped in a confined environment are less likely to move during catalysis, preventing the nucleation or surface reconstruction commonly observed in catalysis and electrocatalysis. This approach can be critical in developing efficient and stable catalysts for electrochemical $CO_2$ reduction. Building on this concept, single-atom transition metals coordinated with nitrogen ($M–N_x$) in carbon-based materials have attracted significant attention due to their superior electrocatalytic properties. The unique structure and coordination environment of the $M–N_x$ units confer favorable kinetics, resulting in excellent activity. Additionally, single-atom catalysts (SACs) maximize the metal utilization, given that each atom serves as an active site, enhancing the efficiency and reducing the need for precious metals. Their precise coordination environments offer high selectivity for the desired products, while their strong anchoring prevents their agglomeration and maintains their stability under the reaction conditions. Furthermore, the tunable electronic properties and simple structure of SACs facilitate mechanism studies and optimization. This versatility extends their application to various electrochemical processes, including hydrogen evolution, nitrogen reduction, and oxygen reduction, making SACs a promising pathway for developing efficient, stable, and cost-effective catalysts.[172–177] MOFs are ideal for constructing SACs due to their high surface area, uniform and tunable pore structures, and strong coordination bonds, ensuring the stable dispersion and isolation of single metal atoms. Additionally, their versatile chemistry and adjustable coordination environment allows for precise tuning of their electronic properties to optimize the catalytic performance.[178–180] However, the commonly reported MOF-based SACs are limited to those with N atoms in their structure, such as ZIFs[181,182] and porphyrinic MOFs.[183,184]

**3.2.1 Nickel-SACs.** A single Ni site catalyst was synthesized based on the ionic exchange between the Zn nodes in the ZIF-8 structure and adsorbed Ni ions within the cavity of the MOF (Fig. 7a).[49] The carbonization of ZIF-8 was carried out at 1000 °C under Ar after treatment with $Ni(NO_3)_2$ aqueous solution, denoted as Ni SAs/N–C. The XPS results revealed the ionic nature of $Ni^{\delta+}$ ($0 < \delta < 2$) in the Ni SAs/N–C and the dominant Ni–N coordination in Ni SAs/N–C, which was confirmed by the extended X-ray absorption fine structure (EXAFS) to be three N and one C coordinated to Ni (Fig. 7b). The electrocatalytic evaluation of Ni SAs/N–C exhibited a more positive onset potential and three times higher current density (10.48 mA $cm^{-2}$ at −1.0 V) relative to Ni NPs/N–C. Furthermore, a lower charge transfer resistance was identified for Ni SAs/N–C in comparison to the Ni NPs/N–C. As can be observed in Fig. 7c, the maximum FE of 71.9% at the potential of −0.9 V was obtained over Ni SAs/N–C. The crucial role of the Ni content was proved based on the diminished current density and FEs of the pyrolyzed ZIF-8 sample and by applying Ni foam as an electrode, which displayed sluggish catalytic activity, producing $H_2$ as the main product. Therefore, it was concluded that the improved $CO_2$ electro-reduction efficiency of Ni SAs/N–C towards CO production is due to its increased number of surface-active sites, enhanced electronic conductivity, and lower CO adsorption energy compared to single Ni sites. However, the drawback of this catalyst was its competitive activity towards HER,[187,188] which significantly decreased the high FE for CO production.

Gong *et al.*[157] prepared Ni single-atom (SA) embedded in N-doped carbon ($Ni_{SA}–N_x–C$) by applying a non-nitrogenous MOF. In their strategy, bimetallic MgNi-MOF-74 was synthesized, in which a large amount of $Mg^{2+}$ assisted in realizing the

Published on 25 August 2024. Downloaded on 02.05.26 08:00:32.

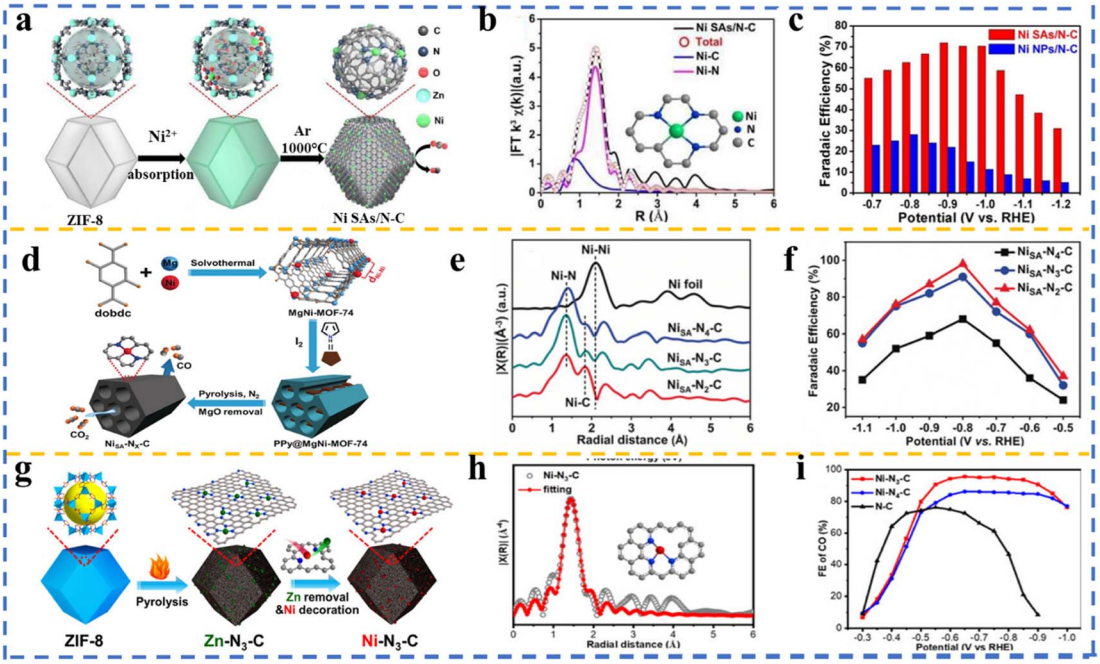


Fig. 7 (a) Schematic of the formation NiSAs/N–C and (b) EXAFS spectra for Ni SAs/N–C. (Inset): proposed structure of Ni–$N_S$. (c) FEs of CO obtained over NiSAs/N–C and Ni NPs/N–C. Reproduced with permission.[49] Copyright 2017, the American Chemical Society. (d) Representative process for synthesizing $Ni_{SA}$–$N_x$–C using bimetallic Mg–Ni-MOF-74. (e) FT-EXAFS spectra of $Ni_{SA}$–$N_x$–C and Ni foil, and (f) faradaic efficiencies of CO. Reproduced with permission.[157] Copyright 2020, Wiley-VCH. (g) Representative process for fabricating Ni–$N_3$–C using ZIF-8 and post-synthetic metal substitution, (h) EXAFS data fitting for Ni–$N_3$–C together with the optimized coordination environment of Ni atoms (inset), and (i) faradaic efficiencies of CO achieved over Ni–$N_3$–C, Ni–$N_4$–C, and N–C. Reproduced with permission.[185,186] Copyright 2021, Wiley-VCH.

isolation of $Ni^{2+}$ in the framework, and the pyrrole monomer was filled in the channels of MOF as the source of nitrogen, producing polypyrrole@MgNi-MOF-74 after *in situ* oxidative polymerization in the presence of $I_2$ (Fig. 7d). Single-atom Ni–N–C was formed upon pyrolysis and MgO was removed by etching. The sample was treated at three different temperatures of 600 °C, 800 °C, and 900 °C, and named $Ni_{SA}$–$N_2$–C, $Ni_{SA}$–$N_3$–C, and $Ni_{SA}$–$N_4$–C, depending on their actual nitrogen ratio, respectively. To elucidate the valence state and coordination environment of $Ni_{SA}$–$N_x$–C ($x = 2, 3, 4$), X-ray absorption spectroscopy (XAS) was employed. It was found that the positive valence of the Ni atom located between $Ni^0$ and $Ni^{2+}$ was also consistent with the XPS results. Moreover, according to the Fourier transform-extended X-ray absorption fine structure (FTEXAFS) spectra, the dominant peaks were assigned to the Ni–N (~1.36 Å) and Ni–C (~1.87 Å) scattering paths, and no peak related to Ni–Ni was observed for all three samples, confirming the formation of single atoms (Fig. 7e). The results of FT-EXAFS revealed the Ni–N coordination numbers of 4.0, 3.4, and 2.0 for $Ni_{SA}$–$N_4$–C, $Ni_{SA}$–$N_3$–C, and $Ni_{SA}$–$N_2$–C, respectively, which are consistent with the N ratio determined through the elemental analysis. Subsequently, to assess the function of the Ni–N coordination environment on the performance of the catalyst, electrocatalytic $CO_2$ reduction over $Ni_{SA}$–$N_x$–C in 0.5 M $KHCO_3$ saturated with $CO_2$ was studied. Noticeably, the current density of $Ni_{SA}$–$N_2$–C was higher than that of its counterparts with an N ratio of 3 or 4. As can be observed in Fig. 7f, this sample afforded the maximum CO FE of 98% at −0.8 V, demonstrating the best electrocatalytic activity among the single-atom Ni–N–C catalysts, revealing that the Ni site coordinated by two nitrogen atoms had the best coordination environment for $CO_2$RR. Also, CO and $H_2$ were identified as the products, and no other carbonaceous products were generated. The much lower current density and $FE_{CO}$ for the Ni–N–C catalyst containing Ni NPs compared to that of $Ni_{SA}$–$N_2$–C demonstrated the privilege of single atom sites. Furthermore, according to DFT calculation, $Ni_{SA}$–$N_2$–C resulted in the lowest free energy barrier for the rate-limiting step (given that $CO_2$RR to CO generally involves a two-proton and two-electron transfer process) and very low CO* desorption energy, which is assumed to affect the catalytic performance of this sample compared to its counterparts.

Although single-atom catalysts (SACs) are known for their exceptional catalytic activity and selectivity, the primary challenge with these catalysts is the rational control of their coordination microenvironment. Thus, to overcome this, Hai-Long Jiang and co-workers presented a general approach for the rational fabrication of low-coordinate single-atom Ni electrocatalysts using MOFs for highly selective $CO_2$ electroreduction. The catalysts were synthesized through a post-synthetic metal substitution (PSMS) strategy, which involved replacing Zn atoms in a Zn-based MOF with Ni atoms to create Ni–$N_3$–C, where each Ni atom is coordinated by three nitrogen atoms (Fig. 7g and h). The PSMS strategy allows precise control of the coordination environment of SACs, overcoming the limitations of the traditional one-step pyrolysis methods. The Ni–$N_3$–C

 This journal is © The Royal Society of Chemistry 2024

Published on 25 August 2024. Downloaded on 02.05.26 08:00:32.

catalyst exhibited an impressive CO FE of up to 95.6% at −0.65 V, which was significantly higher than that of Ni–$N_4$–C (89.2%) and N–C (76.1%) (Fig. 7i). Theoretical calculations revealed that the lower coordination number in Ni–$N_3$–C facilitates the formation of COOH* intermediates, thus accelerating the $CO_2$ reduction process. Furthermore, Ni–$N_3$–C demonstrated robust stability, maintaining high CO selectivity and a current density over 10 h of electrolysis. The Ni–$N_3$–C catalyst was further tested in a Zn–$CO_2$ battery, showing excellent CO selectivity (over 90% at 2 mA) and stability across 100 discharge–charge cycles. This work emphasizes the critical role of the coordination microenvironment in enhancing the catalytic performance of SACs and offers a promising approach for the development of efficient electrocatalysts for $CO_2$ reduction.[185]

**3.2.2 Iron SACs.** An Fe-containing ZIF-8 was employed as a template to prepare mesoporous carbon nanoparticles doped with nitrogen (mesoN–C–Fe), in which iron sites were atomically dispersed *via* high-temperature pyrolysis.[189] Given that the surface area, the number of accessible active sites, and the pore volume of carbon nanoparticles will be reduced as a result of their severe fusion during thermal treatment at high temperatures,[190,191] in the present approach, the hydrolysis of tetramethyl orthosilicate (TMOS) in Fe-ZIF-8 was exploited to obtain NC-Fe@$SiO_2$ after the pyrolysis of ZIF-8-Fe@$SiO_2$, followed by $SiO_2$ etching with NaOH solution. It was demonstrated that $SiO_2$ played a significant role in retaining a large surface area in the mesoporous structure of carbon and hindering the creation of nanoparticles of iron (oxide). Applying a combination of X-ray absorption spectroscopy (XAS) and theoretical calculations, it was deduced that $H_2O$/OH moieties completed the porphyrinic environment around iron (Fe–$N_4$ moiety) in mesoporous NC-Fe. A higher $FE_{CO}$ and $j_{CO}$ were achieved in the electrocatalytic study of mesoN–C–Fe with 85% $FE_{CO}$ at 0.73 V *vs.* RHE compared to the mesoN–C (the catalyst without Fe, $FE_{CO}$ of 72% at $V_{RHE}$ of 0.93 V) and micron-C–Fe (the catalyst without using $SiO_2$, $FE_{CO}$ of 33% at $V_{RHE}$ of 0.93 V). This superior performance of mesoN–C–Fe was explained by considering that more atomically dispersed active sites were available as a result of larger surface area and lower free energy barrier of *COOH and *CO intermediates obtained over the atomically dispersed Fe center coordinating in the porphyrinic environment with OH/$H_2O$, and thus at lower overpotentials, $CO_2$ electroreduction to CO was promoted. Furthermore, it was proven that the single Zn sites in the structure of nitrogen-doped carbon matrix (Zn–$N_x$) promoted the performance of $CO_2$ electroreduction towards CO production, enabling the formation of *COOH.[192,193]

Ye *et al.*[194] prepared single sites of Fe–N on a carbon matrix *via* the pyrolysis of post-modified ZIF-8. In this study, they modified the surface of the as-synthesized ZIF-8 with ammonium ferric citrate (AFC) (as an $Fe^{3+}$ source), and after pyrolysis under an inert atmosphere, C-AFC©ZIF-8 was formed (Fig. 8a). This catalyst exhibited an FE of 89.1% in $CO_2$RR towards CO production, which is attributed to the isolated Fe–N active sites

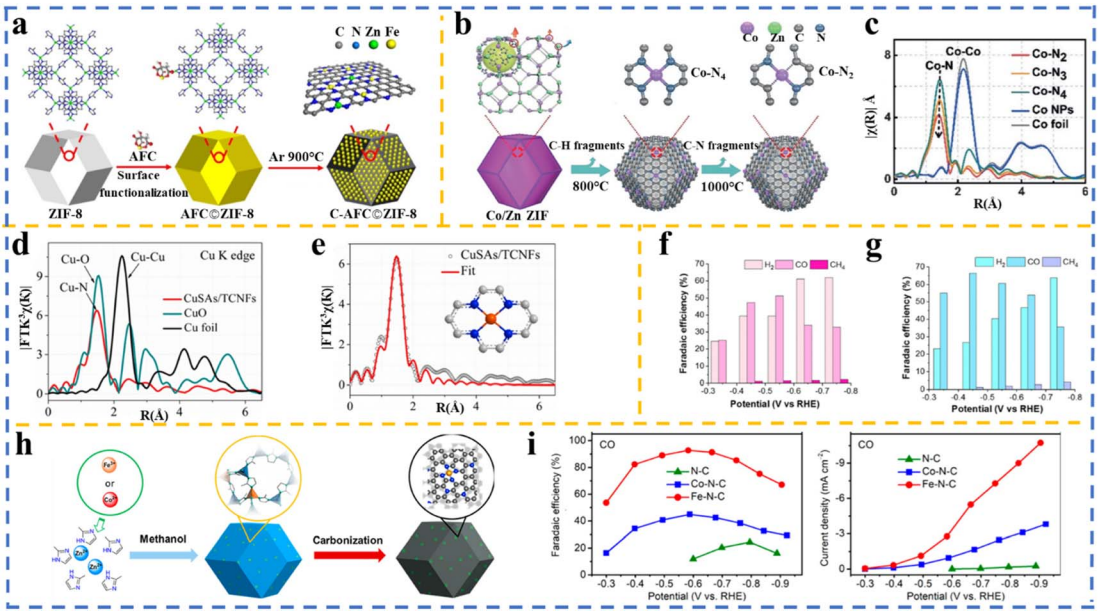


Fig. 8 (a) Schematic of Fe–N doped porous carbon synthesized by adding ammonium ferric citrate (AFC) to as-synthesized ZIF-8, followed by pyrolysis. Reproduced with permission.[194] Copyright 2017, Elsevier. (b) Synthesis process of Co–$N_4$ and Co–$N_2$ active sites using Co/Zn ZIF followed by pyrolysis. (c) EXAFS spectra demonstrating the atomic dispersion of Co atoms in Co–$N_2$, Co–$N_3$, and Co–$N_4$, confirming the lowest N coordination number in Co–$N_2$. Reproduced with permission.[50] Copyright 2018, Wiley-VCH. (d) Fourier transform (FT) at R space showing Cu–N. (e) EXAFS data fitted of CuSAs/TCNFs. Reproduced with permission.[173] Copyright 2019, the American Chemical Society. Electrochemical performance comparison: faradaic efficiency at different applied potentials for (f) $Mn_{SA}$/NC and (g) $Mn_{SA}$/SNC. Reproduced with permission.[195] Copyright 2021, the American Chemical Society. (h) Schematic of the formation of Fe–N–C and Co–N–C using Fe- and Co-doped ZIF-8. (i) Comparative analysis of CO faradaic efficiency and partial current densities across N-doped carbon, Co–N-doped carbon, and Fe–N-doped carbon. Reproduced with permission.[162] Copyright 2018, the American Chemical Society.

Published on 25 August 2024. Downloaded on 02.05.26 08:00:32.

generated on the carbon matrix surface after the pyrolysis, as confirmed by Fourier transformation of the EXAFS analysis.

**3.2.3 Cobalt SACs.** The $CO_2$RR performance of atomically dispersed Co-catalysts containing various coordinated nitrogen was studied by Y. Li and co-workers.[49] The hybrid Co/Zn ZIF was pyrolyzed under an inert atmosphere at 800 °C, 900 °C, or 1000 °C, which resulted in the formation of Co–$N_4$, Co–$N_3$, and Co–$N_2$ species, respectively, as shown in Fig. 8b and c. The Co–$N_2$ sites revealed the best catalytic performance towards CO production with 94% FE and 18.1 mA $cm^{-2}$ current density at −0.63 V *vs.* RHE. This catalyst achieved a CO formation turnover frequency (TOF) of 18 200 $h^{-1}$, surpassing many reported metal-based catalysts under similar conditions. Its high catalytic activity was attributed to its lower coordination number, which facilitated the activation of $CO_2$ to the radical anion intermediate, enhancing the $CO_2$ electroreduction process. Mechanistic insights were gained through experimental and theoretical studies, including DFT calculation and X-ray absorption spectroscopy (XAS). These analyses revealed that reducing the coordination number of Co atoms increases the number of unoccupied 3d orbitals, improving $CO_2$ adsorption and reducing the energy barrier for the formation of the $CO_2^{\bullet-}$ intermediate. This study also found that Co–$N_2$ catalysts exhibit lower charge-transfer resistance and more effective $CO_2$ adsorption compared to Co–$N_4$ catalysts.

**3.2.4 Copper SACs.** Inspired by the findings that incorporating nonprecious metals in nitrogen-doped carbon enhanced the $CO_2$RR performance,[196] Yang *et al.*[173] prepared carbon nanofibers doped with isolated Cu (CuSAs/TCNFs), which have the potential to generate pure methanol with 44% FE. The through-hole structure of the catalyst produced abundant Cu single atoms, thus enhancing its performance. As displayed in Fig. 8d, the FT-EXAFS spectrum of the catalyst showed a dominant Cu–N coordination at 1.48 Å. Furthermore, its EXAFS spectrum (Fig. 8e) can be well-matched with the proposed Cu–$N_4$ structure (see inset).

**3.2.5 Manganese SACs.** Sulfur doping is another strategy to adjust the electronic structures of MOF-derived SACs. Hence, Tan *et al.*[195] studied the sulfurization effect on Mn-based single-atom catalysts derived from MOFs for the electrochemical $CO_2$ reduction reaction. $Mn_{SA}$/NC showed increasing CO production efficiency as the applied potential was lowered, peaking at around 50% FE at −0.55 V before hydrogen evolution began to dominate. In contrast, $Mn_{SA}$/SNC demonstrated a superior catalytic performance, achieving a higher CO FE of 55% at −0.35 V and nearly 70% at −0.45 V, with sustained high CO production across a broader potential range (Fig. 8f and g). Detailed EXAFS fitting revealed that $Mn_{SA}$/NC contained the well-known $MnN_4$ moiety, while $Mn_{SA}$/SNC featured a novel $MnN_3S_1$ moiety. *Operando* XAS experiments suggested that the enhanced performance of $Mn_{SA}$/SNC was not due to the Mn center itself but rather the influence of the sulfur atom. The larger sulfur atom likely induced a twist in the local structure of $MnN_3S$, creating a noncoplanar geometry that may facilitate the formation of S–O bonds, thereby stabilizing the *COOH intermediate crucial for CO production.

**3.2.6 Comparative performance of SACs.** A study by Li and co-workers investigated the structure and reactivity of atomically dispersed M–$N_4$ (M = Fe and Co) sites in electrochemical $CO_2$ reduction. By synthesizing Fe- or Co-doped zeolitic imidazolate frameworks-8 (ZIF-8), followed by thermal activation, nitrogen-coordinated Fe or Co sites atomically dispersed into carbons (M–N–C) were obtained (Fig. 8h).[162] After thermal activation, the dodecahedron shape of the catalysts was preserved, and the HAADF-STEM images demonstrated that the Fe and Co atomic sites were well-dispersed and embedded in the carbon matrix at the edge sites. Generally, in the heat treatment of Fe-, N-, and C-containing precursors, two types of Fe–$N_4$ could be generated, including bulk-hosted Fe–$N_4$ moieties embedded in the bulk graphitic layer (entirely encapsulated by carbon atoms),[197] and edge-hosted Fe–$N_{2+2}$, indicating that an Fe atom was connected to two N atoms at the edges of each graphitic layer and bonded to two N-doped graphitic layers.[198] The coexistence of both Fe–$N_{2+2}$–$C_8$ and Fe–$N_4$–$C_{10}$ in the Fe–N–C catalyst was verified by Mössbauer spectroscopy (these numbers of carbon atoms indicate the number of C-atoms considered in the model of DFT calculations and proposed as possible site candidates). The electrochemical $CO_2$ reduction activity of these catalysts was tested, which exhibited that they follow the order of Fe–N–C > Co–N–C > N–C to produce CO, in which the FE of 93% was achieved over Fe–N–C (Fig. 8i). The role of the edge-hosted M–$N_{2+2}$–$C_8$ moieties as the active sites in the reduction of $CO_2$ was clarified by DFT calculations.

Jiao *et al.*[199] presented a general approach for the synthesis of single-atom metal embedded in N-doped carbon ($M_1$–N–C; M = Fe, Co, Ni, and Cu) by pyrolyzing porphyrinic multivariate metal–organic frameworks (MTV-MOFs) named M-PCN-222 (M = Fe, Co, Ni, and Cu), which was assembled through the mixed ligand approach by employing M-TCPP (M = Fe, Co, Ni, and Cu) and $H_2$-TCPP, as shown in Fig. 9a. As can be observed in Fig. 9b, single atoms were formed given that no Ni–Ni peak was detected. Interestingly, in the electrochemical reduction of $CO_2$, a very high CO FE of 96.8% at −0.8 V was achieved over $Ni_1$–N–C, outperforming Fe-, Co-, and Cu-based $M_1$–N–C (Fig. 9c). Searching for the reason for the high catalytic performance of the $Ni_1$–N–C catalyst, DFT calculations presented that the rate-determining step for all the $M_1$–N–C catalysts is the formation of *COOH and $Ni_1$–N–C and $Fe_1$–N–C exhibited much lower energy barriers for *COOH compared the other two catalysts. Moreover, a much lower energy barrier for CO desorption was calculated for the $Ni_1$–N–C catalyst. A more positive value of $U_L(CO_2) - U_L(H_2)$ limiting potential difference between $CO_2$RR and HER ($U_L(CO_2) - U_L(H_2)$; $U_L = -\Delta G_0/e$) was measured for $Ni_1$–N–C, suggesting its higher $CO_2$RR selectivity than hydrogen evolution.[201]

The synthesis of $Fe_1$–$Ni_1$–N–C was achieved by pyrolyzing ZIF-8 with Fe and Ni-doped ZnO nanoparticles. This process revealed neighboring Fe and Ni single sites, showcasing an impressive faradaic efficiency of 96.2% for CO production in the electroreduction of $CO_2$.[52] Subsequently, Zhang *et al.*[203] devised Ni–N–C through the *in situ* addition of an Ni precursor to the precursor solution of ZIF-8, with the addition of cetyltrimethylammonium bromide (CTAB), followed by the pyrolysis of ZIF-8@CTAB@$Ni^{2+}$. In the electrochemical reduction of $CO_2$, Ni–N–C demonstrated an outstanding faradaic efficiency of

 This journal is © The Royal Society of Chemistry 2024

Published on 25 August 2024. Downloaded on 02.05.26 08:00:32.

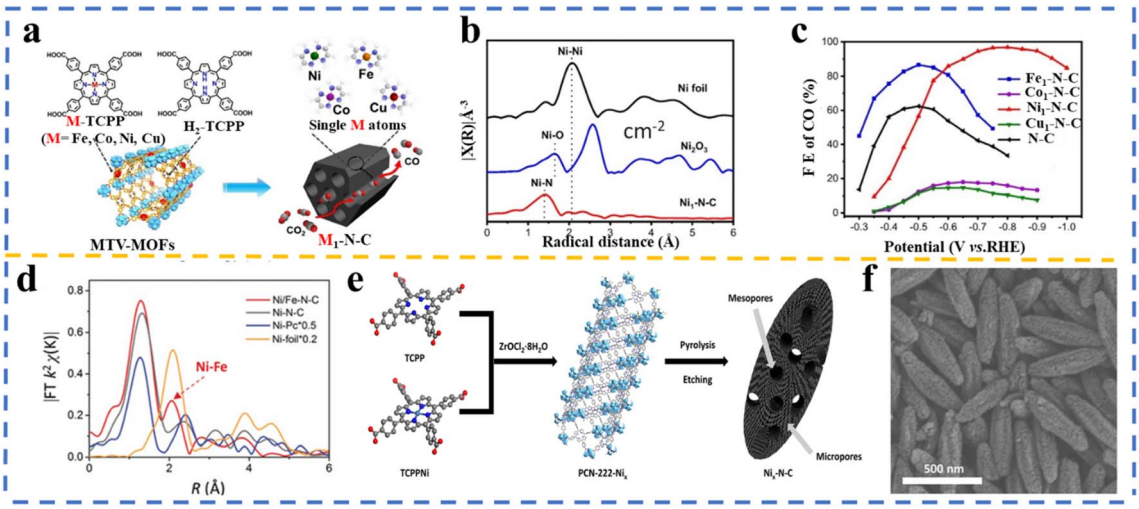


Fig. 9 (a) Schematic of the synthesis Fe-, Co-, Ni-, Cu–N–C based on multivariate metal–organic frameworks (MTV-MOFs); (b) $k^2$-weighted FT-EXAFS spectrum and (c) faradaic efficiency of CO obtained over $Ni_1$–N–C, $Fe_1$–N–C, $Co_1$–N–C, $Cu_1$–N–C. Reproduced with permission.[200] Copyright 2020, Wiley-VCH. (d) Fourier transform (FT) $k^2$-weighted $\chi(k)$ function of the extended X-ray absorption fine structure (EXAFS) spectra. Reproduced with permission.[201] Copyright 2019, Wiley-VCH. (e) Schematic of $Ni_x$–N–C using Zr-based MOF (PCN-222) and (f) SEM image of $Ni_{20}$–N–C. Reproduced with permission.[202] Copyright 2020, the American Chemical Society.

98% towards CO. It was inferred that the Ni–$N_x$ sites favored $CO_2$ activation, enabling the adsorption of *CO and the establishment of *COOH intermediates.

### 3.3 MOF-derived nitrogen- and metal–nitrogen-doped porous carbon catalysts

Metal–nitrogen (M–N)[204] and metal–nitrogen-grafted porous carbon (M–N–C)[205] derived from MOF materials have attracted substantial attention in $CO_2$RR. These M–N and M–N–C materials contain coordinatively unsaturated transition metal–nitrogen sites known as single-atom electrocatalysts.[176,177,206–208] The catalytic performance of these sites is highly affected by the coordination environments and the types of metal centers.

Wang *et al.*[165] prepared N-doped carbon catalysts employing ZIF-8 as a sacrificial template for $CO_2$RR after etching with acid. In this study, ZIF-8 was carbonized at three different temperatures (700 °C, 800 °C, and 900 °C) denoted as NC-T, with $T$ representing the temperature. Subsequently, the characteristics and electrocatalytic activity of these three samples were investigated. The evaluation revealed that the sample pyrolyzed at the highest temperature exhibited the greatest FE toward CO production, with NC-900 achieving the highest CO FE of approximately 78% at −0.93 V *vs.* RHE. In addition, the partial current density for CO ($j_{CO}$) and the highest total current density ($j_{total}$) were also recorded for the NC-900 sample. Raman spectroscopy revealed that the carbon matrix in both NC-800 and NC-900 has equivalent degrees of graphitization, while NC-700 demonstrated an overestimated ratio between the G and D bands of carbon, which was ascribed to the non-pyrolyzed imidazolate.[209] It was noted that the surface area of the samples increased by increasing the pyrolysis temperature, suggesting that more residuals were removed from the pores at high temperatures; however, it also led to more agglomeration of the carbon nanoparticles. Furthermore, the study of the N 1s XPS region manifested the presence of four types of nitrogen species, pyridinic-N, pyrrolic-N, quaternary-N, and oxidized-N, respectively.[210] Interestingly, as the pyrolysis temperature increased, the nitrogen content decreased, and in all three samples, the dominant N-species was pyridinic-N. When iron was introduced through the ammonia treatment of ammonium ferric citrate post-modified ZIF-7, a significant improvement in catalytic performance was achieved. The optimized catalyst demonstrated a higher faradaic efficiency (~85% at −0.43 V *vs.* RHE) and an increased partial current density for CO production (17.8 mA $cm^{-2}$ at −0.83 V *vs.* RHE). The XPS results exhibited the presence of five nitrogen configurations, including pyridinic-N, metal–N, pyrrolic-N, graphitic-N, and *N*-oxidized in the N 1s peak. Interestingly, the amount of pyridinic-N was suppressed in the catalyst showing the highest performance. It was demonstrated that employing $NH_3$ gas augmented the surface and mesoporous areas by promoting the removal of Zn and minimizing the unstable carbon moieties. Altering the $NH_3$ flow and pyrolysis time influenced the current density and CO faradaic efficiency.[211]

Ren *et al.*[201] synthesized nitrogenated carbon embedded with isolated bimetallic Ni–Fe sites (Ni/Fe–N–C) employing a Zn/Ni/Fe zeolitic imidazolate framework as the precursor, which was investigated as an electrocatalyst for $CO_2$RR. Fe was chemically bonded to the organic ligand in the original MOF, and Ni was capsulated in the framework, as shown in Fig. 9d. A faradaic efficiency of >90% and high selectivity towards CO within a broad potential range of −0.5 to −0.9 V *vs.* RHE were achieved. DFT calculation demonstrated that by applying the Ni/Fe–N–C catalyst, the energy barrier for the formation of the COOH* intermediate and CO desorption was diminished in comparison to the Ni–N–C and Fe–N–C catalysts, showing the synergistic effect of the bimetal nitrogen sites.

Published on 25 August 2024. Downloaded on 02.05.26 08:00:32.

Ni–N–C, Co–N–C, and Fe–N–C as non-noble metal–nitrogen-doped carbon catalysts are relatively inexpensive and have excellent selectivity towards CO production.[178,212,213] However, Ni–N–C requires higher overpotentials, and its CO selectivity is more prominent compared to the other two catalysts.[212,214] According to these findings, the stable porphyrin-based porous Zr-MOF (PCN-222) was exploited as a sacrificial template to prepare a hierarchical nanoporous Ni–C–N catalyst (Fig. 9e and f).[202] This catalyst contained microporous structures originating from its interconnected mesopores and the nano-MOF precursor produced during pyrolysis. To verify the nature of the main active species (in some cases, Ni nanoparticles,[215,216] and in other cases Ni–N–C[178,213,217] were reported as the active catalytic sites), DFT simulation[212] was utilized and Ni nanoparticles were proposed as the most favorable active sites for the HER process. Moreover, the measured Tafel slope for $j_{CO}$ over the Ni–N–C catalyst confirmed that the rate-determining step (RDS) should be the first electron transfer, signifying the Ni–N–C species as the active sites. Although the RDS assigned to the Ni NPs led to a much higher Tafel slope for the $CO_2$ reduction reaction than Ni–N–C active site, the evaluation of the Ni–N–C catalyst synthesized with different molar ratios of TCPP (*meso*-tetra(4-carboxyphenyl)porphyrin) and TCPPNi indicated that a small content of Ni NPs is favorable for improving the catalytic performance given that it was reported in the literature that Ni–N–C was the main active site.

In the search for catalysts for the selective reduction of $CO_2$ to hydrocarbons and alcohols, Cu metal is considered an ideal catalyst.[218] Usually, the hybridization of Cu with carbon materials such as carbon black[219] and MOF-derived porous carbon[220] can be realized to create more catalytic active sites. However, the local field around Cu is effective in enhancing the $CO_2$RR.[221] Cheng *et al.*[222] studied the effects of N-doping on $CO_2$RR by employing a series of N-containing ligand (benzimidazole, BEN) modified Cu-BTC (1,3,5-benzene tricarboxylic acid) MOFs carbonized at three different temperatures. It was shown that the average size of the Cu nanoparticles increased by enhancing the annealing temperature from 400 °C to 800 °C. The high-resolution N 1s spectrum revealed five peaks associated with pyrrolic-N, pyridinic-N, graphitic-N, Cu–N, and oxidized-N, where increasing the annealing temperature decreased the amount of Cu–N and pyrrolic-N. According to the notably high $CO_2$ electrochemical reduction activity and selectivity toward ethylene and ethanol obtained over the sample carbonized at 400 °C, it was deduced that Cu–N and pyrrolic-N play a major role in $CO_2$RR, while for the sample carbonized at 800 °C, HER was substantially suppressed. Although the aggregation of Cu atoms into large-size nanoparticles results in a decrease in the amount of active sites, which is one of the challenges of copper-containing catalysts, Xuan *et al.*[223] prepared bimetal pyrolyzed ZIF of Cu and Zn, in which the atoms did not aggregate. Incorporating Zn atoms in Cu ZIFs helped suppress the aggregation of the atoms and elevated the formation of active sites. By altering the Cu and Zn ratio, the $Cu_1Zn_1$–N–C catalyst showed 95.6% $CH_4$ selectivity in the $CO_2$ reduction reaction. It was shown that the Zn atoms played a role in preventing metal aggregation in the carbonization step, which enhanced the vacancy-copper–nitrogen (V-Cu–N) active sites. The results of the X-ray absorption spectroscopy (XAS) measurement unveiled that the catalysts contained many vacancy-metal–nitrogen active sites (V-Cu–N and V-Zn–N sites), and according to DFT simulations, the V-Cu–N sites remarkably increased the selectivity toward $CH_4$.

Multilayer N-doped graphene embedded with Ni–N–C active sites was synthesized using amino-functionalized Ni-based MOF ($NH_2$–Ni-MOF) as a precursor.[224] During annealing at 1000 °C and acid treatment, the $-NH_2$ group in the MOF precursors induced more structural defects and edge plane exposure on the graphene layers,[225] thus generating more abundant Ni–N–C sites. The catalyst demonstrated remarkable $CO_2$ electrochemical activity towards CO with the maximum FE of 97% at a low overpotential of 0.79 V, which is assigned to the combined effect of the abundant Ni–N–C sites and slight amount of encapsulated Ni cores.[224]

Using an $NH_2$-containing Ni/Zn bimetallic MOF precursor ($NH_2$–$ZnNi_{1/x}$-MOF) with varying ratios of Ni/Zn, Wang *et al.*[226] prepared Ni nanoclusters highly dispersed on N-doped carbon. The Ni/Zn ratio and the $-NH_2$ group of the ligand in the MOF structure influenced the size of the Ni catalyst. After pyrolysis of the MOF precursor at 1000 °C, the $NH_2$–$ZnNi_1$/150-MOF sample (Ni/Zn ratio of 1 : 150) contained an average Ni nanocluster of 1.9 nm grafted on pyridinic N-rich carbon. During the electrochemical conversion of $CO_2$ to CO, the catalyst exhibited an FE of 98.7% and current density of $-40.4$ mA cm$^{-2}$. The exceptional long-term stability of the material/catalyst was attributed to the synergistic effect of small Ni clusters and their optimum interaction with the carbon support.

**3.3.1 The role of N-species of N-doped carbon materials in electrochemical reduction of $CO_2$.** It has been demonstrated that nitrogen-doped carbon materials show a higher tendency to interact with $CO_2$ compared to carbon materials. In this case, N-doped carbon materials are considered effective to boost the $CO_2$ storage capacity and $CO_2$ reactivity. The interaction of $CO_2$, a Lewis base, with carbon-doped N materials, is classified as a Lewis/base reaction.[227] Carbon-doped N materials, a new class of heteroatomic, metal-free heterogeneous catalysts, have shown their merits in $CO_2$RR. N-doped carbon materials can be the most promising substitute for noble metal catalysts in this area owing to their high surface areas, electrochemical activity, low cost, and tunable conductivity.[228,229] Furthermore, N-doped carbon materials seem appealing in $CO_2$RR due to their capacity to reduce the competing $H_2$ evolution reaction.[230,231] N-doped carbon fibers, graphene, carbon nanotubes, and nanodiamonds are various types of N-doped carbon materials that are investigated in $CO_2$RR.[232–234] Thus far, various studies have explored the role of N-species in N-doped carbon materials applied in $CO_2$RR; however, the discussion still needs to be completed. Based on XPS investigation and stability tests, Kumar *et al.*[228] suggested that reduced carbon atoms are responsible for reducing $CO_2$ rather than nitrogen atoms. Zhang *et al.* proposed that the graphene $\pi$ system makes N atoms negatively charged, whereas carbon atoms are positively charged. By adsorbing $CO_2$ onto N atoms, its reduction to $CO_2^{\bullet-}$ occurs at a considerably reduced overpotential.[231] Using DFT

 This journal is © The Royal Society of Chemistry 2024

Published on 25 August 2024. Downloaded on 02.05.26 08:00:32.

and *ab initio* molecular dynamic calculations, Chai *et al.* proposed that graphitic/quaternary nitrogen atoms are the active sites.[235] Subsequently, Xu *et al.* proposed that the formation of $CO_2^{\bullet-}$ occurs through the initial rate-determining transfer of one electron to $CO_2$ and nitrogen atoms, especially quaternary and graphitic nitrogen, favoring the stabilization of the $CO_2$ radical anion.[232] From another point of view, several studies demonstrated that the N defects in the hexagonal graphitic networks are most likely the active sites in $CO_2$RR on N-doped carbon materials.[210,229,236–239]

To date, MOFs have been widely explored as hard templates to form N-doped porous carbons employed as heterogeneous catalysts in various reactions,[10,240–242] including the electrochemical reduction of $CO_2$. To gain insights into the active sites, Ye *et al.*[48] proposed that pyridinic nitrogen is the active site according to XPS results for N-doped carbon prepared from Zn-MOF-74 and DFT calculations. Four types of nitrogen including pyridinic, pyrrolic, graphitic, and nitrogen oxide were recognized in the high-resolution N 1s XPS on their samples. The amount of nitrogen species was controlled by the calcination temperature. It was shown that there is a relationship between the total pyridinic and graphitic N and the maximum FE for CO. Furthermore, DFT calculations based on the potential limiting steps (PLS) of $CO_2$RR on the surface of the catalyst and the Gibbs free energy changes demonstrated the minor energy barrier for pyridinic N (Fig. 10a). Wang *et al.*[165] also proposed the high catalytic performance of an N-doped carbon catalyst prepared *via* the pyrolysis of ZIF-8, which was attributed to the domain of quaternary and pyridinic nitrogen species in the carbon structure. Based on DFT calculation, Yang *et al.*[173] suggested that Ni–$N_4$ and Cu–$N_4$ demonstrate lower energy to convert $CO_2$ molecules to *COOH (intermediate) in the rate-determining step (RDS) than pyridinic N (Fig. 10b). In contrast, Cheng *et al.*[222] proposed that Cu–N and pyrrolic N in the carbon matrix are active sites, which enhance the adsorption of $CO_2$ and favor C–C coupling to generate ethylene and ethanol on the surface of Cu. Several studies, relying on both experimental and DFT calculations, demonstrated that metal–N in the carbon structure formed from the pyrolysis of MOFs are active sites in $CO_2$ electrochemical reduction rather than other nitrogen species in the carbon structure.[186,223,224]

### 3.4 MOF-derived metals, metal oxides and metal composites

Given that MOFs exhibit low thermodynamic stability under the reduction potential, additional processes have been applied to convert MOFs to functional materials, including metal and metal oxide nanoparticles, which both inherit some structural properties of MOFs and exhibit electrochemical stability.[243] Recent studies demonstrated that the particle size of Cu nanoparticles can highly affect the results of $CO_2$ reduction for methane production.[244,245] In search of novel catalysts to convert $CO_2$ to alcohols electrochemically combining both high efficiency and high stability, Zhao *et al.*[246] carbonized a Cu-based MOF (HKUST-1) to achieve an oxide-derived Cu/carbon catalyst (OD Cu/C). Carbonization of HKUST-1 at three different temperatures of 900 °C, 1000 °C, and 1100 °C resulted in a porous carbon matrix embedded with the oxide-derived Cu nanoparticles, denoted as OD Cu/C-900, OD Cu/C-1000, and OD Cu/C-1100, respectively. $Cu_2O$ was identified in the PXRD pattern of the three samples (given that $Cu_2O$ was determined to be an essential contributor in the production of methanol at a low overpotential),[247,248] and SEM analysis showed that with an increase in the carbonization temperature, the size of the Cu nanoparticles increased. Among them, the OD Cu/C-1000 catalyst showed the highest current density 1.0 mA $cm^{-2}$ at −0.5 V (*vs.* RHE) compared to the samples carbonized at 900 °C and 1100 °C. Moreover, a relatively lower charge transfer resistance was obtained for the OD Cu/C-1000 catalyst through electrochemical impedance spectroscopy (ESI) tests. Notably, the highest production rate of alcohol was obtained over the OD Cu/C-1000 catalyst. The higher activity of the OD Cu/C-1000 catalyst compared to the two other catalysts was ascribed to the smaller charge transfer residence, the higher $Cu_2O$ content, and the well-dispersed copper in the porous carbon matrix.

An Ag/$Co_3O_4$ nanocomposite was prepared *via* the pyrolysis of an Ag/Co-based mixed-metal MOF $[Ag_4Co_2(pyz)PDC_4][Ag_2Co(pyz)_2PDC_2]$ at high temperature in air, which exhibited excellent activity in $CO_2$RR.[249] The FE for CO reached 55.6% over this catalyst in a $KHCO_3$ aqueous solution of 0.1 M, which was much higher than that obtained over $Co_3O_4$. This superior catalytic performance was assigned to the Ag species, which increased the electrical conductivity, accelerated the electron

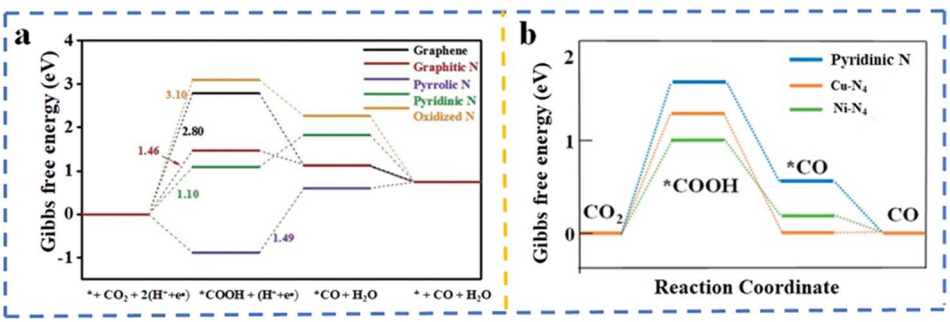


Fig. 10 (a) Production of CO from $CO_2$ reduction in a two-proton and coupled electron pathway, * + $CO_2$ + $H^+$ + $e^-$ → *COOH, *COOH + $H^+$ + $e^-$ → *CO + $H_2O$, *CO + $H_2O$ → * + CO + $H_2O$. Reproduced with permission.[48] Copyright 2020, Wiley-VCH. (b) Reduction of $CO_2$ to CO comparing the Gibbs free energy on pyridinic N, Cu–$N_4$, and Ni–$N_4$. Reproduced with permission.[173] Copyright 2019, the American Chemical Society.

Published on 25 August 2024. Downloaded on 02.05.26 08:00:32.

transport rate, and enhanced the selectivity of the electrode materials toward CO production.

A Cu-based MOF (MOF-74) was converted into isolated Cu NP clusters to obtain efficient electrocatalysts for methane production.[250] Cu NPs are known to agglomerate, and their high loading usually increases the FE for $C_2$ and $C_3$ products.[245] When the porous structure of Cu-MOF-74 was used as a template to generate highly isolated Cu NP clusters, these MOF-derived Cu NPs exhibited outstanding electrocatalytic performances with a high $CH_4$ faradaic efficiency (>50%), which was 2.3 times higher than the commercial Cu NPs.

Liu *et al.*[251] designed copper nanoparticles derived from a Cu-metal organic framework (Cu-MOF/NP) containing Cu as the metal center and 1,3,5-benzenetricarboxylic acid ($H_3BTC$) as the organic linker for $CO_2$ electrochemical reduction to CO in a new flow electrochemical reactor integrated with a membrane electrode assembly (MEA). This Cu-MOF/NP catalyst contained $Cu/Cu_2O$ particles with a porous octahedral structure, including $Cu^0$ and $Cu^+$ catalytic active sites. The XPS and XRD results revealed that an increase in the heating rate favored the formation of the $Cu^+$ chemical state, which further resulted in higher catalytic activity.

Porous Cu nanoribbons, obtained through the *in situ* electrochemical reduction of Cu-MOF with two distinct organic ligands in their structure, exhibited an impressive FE of 82.3% for $C_{2+}$ production with a partial current density of 347.9 mA $cm^{-2}$. This surpasses the performance of Cu nanorods and Cu nanoleaves. The mesoporous structure of the Cu nanoribbons enhanced the electric field on their surface, promoting the concentration of $K^+$ and $OH^-$ ions at the active sites. This ion concentration facilitated the formation of CO intermediates and C–C coupling, thereby lowering the thermodynamic barriers and improving the selectivity for $C_{2+}$ products during $CO_2$ electroreduction. These findings highlight the potential of tuning the selectivity of $C_{2+}$ products through the introduction of mesoporosity in copper catalysts.[51]

It is known that metal oxides of earth-abundant elements such as $In_2O_3$, $SnO_2$, and $Bi_2O_3$ are not only cheap but also have high overpotentials for $H_2$ generation, which may be advantageous for $CO_2$ reduction.[252–254] In this case, combining these metal oxides with other active metals can enhance the selectivity and efficiency of the product formation in $CO_2$RR. A series of In–Cu bimetallic oxides derived from an MOF was prepared by introducing $In_2O_3$ in the structure of a Cu-based MOF.[255] By tuning the ratio of Cu/In in the MOF precursor, the production ratio of $CO/H_2$ could be controlled. In the synthesis procedure, after calcination at 400 °C in air, the resulting In–Cu bimetallic oxide was electrochemically reduced to convert $Cu^{2+}$ to $Cu^{1+}$. The presence of $Cu^{1+}$, which plays a vital role in the formation of CO from $CO_2$, was supported by XRD, XPS, and HR-TEM. It was shown that with an increment in the Cu ratio, the morphology changed from needle-like to cubic, and the surface area also increased. By testing the $CO_2$ electrochemical activity of the In–Cu bimetallic oxides in a 0.5 M $KHCO_3$ aqueous solution saturated with $CO_2$, CO and $H_2$ were recognized in the gas phase. Simultaneously, no liquid product was found in the applied potential range (−0.5 V to −1.0 V *vs.* RHE). The In–Cu bimetallic oxide with a Cu/In ratio of 0.92 displayed the highest current density of 11.2 mA $cm^{-2}$ and $FE_{CO}$ of 92.1% due to its higher electrochemical surface area, porous structure for mass diffusion, lower charge transfer resistance, stronger $CO_2$ adsorption, and synergistic effect between In oxides and Cu oxides.

A copper phosphide/carbon ($Cu_3P/C$) hybrid was synthesized *via* the pyrolysis of $NaH_2PO_2$ and HKUST-1 under Ar at 350 °C.[256] These $Cu_3P/C$ nanocomposites exhibited an FE of 47% CO at a relatively low potential (−0.3 V). Further, when the catalyst was explored as a cathode in an asymmetrical-electrolyte Zn–$CO_2$ battery, it showed a good performance with an open-circuit voltage of 1.5 V and a power density of 2.6 mW $cm^{-2}$ at 10 mA $cm^{-2}$. These promising catalytic properties are likely due to the synergistic interaction between copper and phosphorus, together with the unique structure of $Cu_3P$.

By carbonizing Cu-BTC MOF at controlled temperatures (700 °C, 800 °C, and 900 °C), nitrogen-doped porous carbon frameworks anchored with $Cu_2O/Cu$ nanoparticles ($Cu_2O/Cu$@NC) were prepared.[257] CV scanning in $CO_2$-purged $KHCO_3$ (0.1 M) electrolyte showed the superior performance of the catalyst carbonized at 800 °C, $Cu_2O/Cu$@NC-800, which exhibited the best catalytic activity and formate selectivity with FE of 70.5% (at −0.68 V *vs.* RHE). It was found that increasing the carbonization temperature enhanced the Cu content, specific surface area, and pore volume. The Cu content was enhanced by 36.3% as the carbonizing temperature increased from 700 °C to 800 °C, and it was noteworthy that the amount of $Cu^0$, known as the active site in generating formate, also increased. The higher temperature treatment removed more organic residue from the pores and precursor, leading to an enhancement in the specific surface area and pore volume. Furthermore, studying the effect of N-doping in the catalyst in the selectivity, it was recognized that the higher content of Cu–N–Cu in $Cu_2O/Cu$@NC-800 was beneficial for formate production. In comparison, the selectivity towards ethanol was enhanced over $Cu_2O/Cu$@NC-900 due to its lower content of Cu–N–Cu. It was proposed that there are two main intermediates in $CO_2$ electroreduction, as follows (1) *OCHO and (2) *COOH, which will be reduced to formate or CO, respectively. Here, it appears that N-doping assists formate production by lowering the binding energy of *OCHO.[258] The $Cu_2O/Cu$@NC-800 catalyst exhibited long-term stability of 30 h, which was ascribed to its well-dispersed $Cu_2O/Cu$ nanoparticles, higher Cu content, and higher content of N doped in the $Cu_2O/Cu$ lattice.

As the first example of applying a 2D MOF in $CO_2$RR, copper(II)-5,10,15,20-tetrakis(4-carboxyphenyl)porphyrin–Cu(II) ($Cu_2$(CuTCPP)) nanosheets[46] were utilized, in which there were two different copper chemical environments for selective and efficient $CO_2$ electroreduction to generate acetate and formate. One Cu was the Cu paddle wheel, which was the cluster in the structure of HKUST-1 (effective in $CH_4$ and $C_2H_4$ production),[119] and the other was porphyrinic Cu, known as an electrocatalyst for $CH_4$ formation.[119] The $CO_2$ electrochemical reduction performance of $Cu_2$(CuTCPP) nanosheets on an FTO electrode was analyzed in a solution of $CH_3CN$ containing $H_2O$ and 1-ethyl-3-methylimidazolium tetra-fluoroborate ($EMIMBF_4$) ionic liquid as the supporting electrolyte. To control the

 This journal is © The Royal Society of Chemistry 2024

Published on 25 August 2024. Downloaded on 02.05.26 08:00:32.

concentration of protons and increase the solubility of $CO_2$, an organic electrolyte with water and the ionic liquid were employed,[62,259] and compared to CuO, $Cu_2O$, Cu, and CuTCPP, the cathodized Cu-MOF nanosheets demonstrated remarkable activity toward the production of formate with an FE of 68.4% at a potential of −1.55 V *vs.* $Ag/Ag^+$. The Cu catalyst revealed negligible $CO_2RR$ activity, producing CO and $CH_4$ (FE of 5%) with no formate and acetate detected. Applying CuTCPP as an electrocatalyst generated CO with an FE of 20% at potentials in the range of −1.50 V to −1.65 V, and $H_2$ was identified as the major product. In contrast, HCOOH (with FE of 14.7% at −1.5 V) and $CH_3COOH$ (with FE of 5.8% at −1.45 V) were produced over CuO, while only HCOOH was detected with $Cu_2O$ with an FE of up to 21.5%. Furthermore, the structural changes in the Cu(II) paddle-wheel nodes during cathodized reconstruction to CuO, $Cu_2O$, and $Cu_4O_3$ were confirmed by *ex situ* XRD, SEM, HR-TEM, and XPS.

A Bi-based MOF was studied in the electrochemical reduction of $CO_2$ to formate by Lamagni *et al.*[260] It was demonstrated that Bi(1,3,5-tris(4-carboxyphenyl)benzene) Bi(btb), known as CAU-7,[261] works as a pre-catalyst and at the reducing potentials, where it undergoes structural rearrangement to form the highly active and selective catalyst of porous organic matrix dispersed with Bi-based nanoparticles. Interestingly, this rearrangement happening *in situ* during the electrocatalytic reaction enabled the poor conductivity and instability of the MOF to be overcome. Cyclic voltammetry of Bi(btb) deposited on GC recorded under Ar and $CO_2$ atmospheres in an aqueous solution of 0.5 M $KHCO_3$ indicated the structural transformation of Bi(btb) to a steady state of different Bi species for formate production with an FE of 68.4% at a potential of −1.55 V *vs.* $Ag/Ag^+$. The Cu catalyst revealed negligible $CO_2RR$ activity, producing CO and $CH_4$ (FE of 5%) with formate and acetate detected. Applying CuTCPP as an electrocatalyst generated CO with an FE of 20% at potentials in the range of −1.50 V to −1.65 V, and $H_2$ was identified as the major product. Alternatively, HCOOH (with FE of 14.7% at −1.5 V) and $CH_3COOH$ (with FE of 5.8% at −1.45 V) were produced over CuO, while only HCOOH was detected with $Cu_2O$ with an FE of up to 21.5%. Furthermore, the structural changes in the Cu(II) paddle-wheel nodes during cathodized reconstruction to CuO, $Cu_2O$, and $Cu_4O_3$ were confirmed by *ex situ* XRD, SEM, HR-TEM, and XPS.

A Bi-based MOF was studied in the electrochemical reduction of $CO_2$ to formate by Lamagni *et al.*[260] It was demonstrated that Bi(1,3,5-tris(4-carboxyphenyl)benzene) Bi(btb), known as CAU-7,[261] works as a pre-catalyst and at reducing potentials, it undergoes a structural rearrangement to form the highly active and selective catalyst of porous organic matrix dispersed with Bi-based nanoparticles. Interestingly, this rearrangement happening *in situ* under electrocatalytic reaction resulted in overcoming the poor conductivity and instability of the MOF. Cyclic voltammetry of Bi(btb) deposited on GC recorded under Ar, and $CO_2$ atmosphere in an aqueous solution of 0.5 M $KHCO_3$ indicated the structural transformation of Bi(btb) to a steady state of a different Bi species upon multiple cycling of the $Bi^{3+}/Bi^0$ redox couple (Fig. 11a)[262] which then leads to the Bi-based nanoparticle formation as indicated by grazing-incidence X-ray diffraction, HR-TEM, and XPS. In bulk electrolysis experiments, formate was recognized as the main product with a faradaic efficiency of 95% at an overpotential of 770 mV (Fig. 11b). The discussed MOF-derived materials applied in $CO_2RR$ are summarized in Table 3.

## 4. Active sites and mechanism of MOF-based materials for electrochemical $CO_2RR$

As discussed earlier, MOFs,[39] which are highly ordered coordination polymers, are incredibly appealing materials for several catalytic reactions due to their unique features, combining that of homogenous and heterogeneous catalysts. MOFs have a well-defined structure and highly active catalytic sites incorporated into a stable scaffold, enabling excellent catalytic activity and selectivity, which are crucial parameters in catalysis. Further, their porous structure enables excellent and tunable mass transfer to and from the active sites. Unlike traditional heterogeneous catalysts, the environment around the active sites can

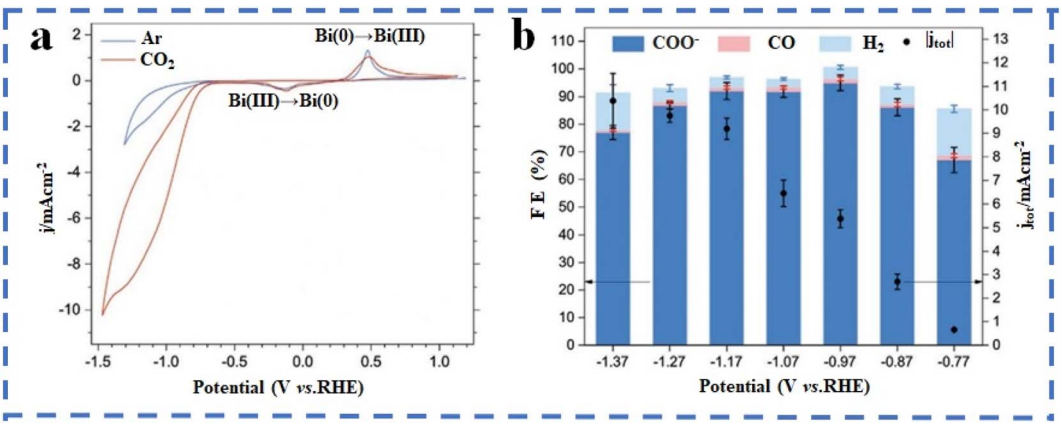


Fig. 11 (a) Multiple cycling of the $Bi^{3+}/Bi^0$ redox couple under Ar and $CO_2$. (b) Faradaic efficiency of the electrocatalysis products at different potentials. Reproduced with permission.[260] Copyright 2020, Wiley-VCH.

Published on 25 August 2024. Downloaded on 02.05.26 08:00:32.

Table 3 Electrocatalytic reduction of $CO_2$ catalyzed by metal–organic framework-derived materials

| Electrocatalyst | Applied MOF | Potential | Electrolyte | Catalytic efficiency (%) | Ref. |
|---|---|---|---|---|---|
| N-doped porous carbon | ZIF-8-supported MWCN[a] | −0.56 V *vs.* RHE | 0.1 M $NaHCO_3$ | $FE_{CO} = 100$ | 166 |
| N-doped porous carbon | Zn-MOF-74 | −0.55 V *vs.* RHE | 0.5 M $KHCO_3$ | $FE_{CO} = 98.4$ | 48 |
| Bi@N-doped porous carbon | ZIF-67 | −1.5 V *vs.* SCE | 0.1 M $KHCO_3$ | $FE_{formate} = 92$ | 167 |
| Dendritic $Cu^0$ and nanowires $Cu^0$ | Cu-MOF | −1.85 *vs.* Ag/AgCl | (0.5 M) $BmimBF_4$/ (1.0 M) acetonitrile/ $H_2O$ | $FE_{formate} = 98.2$ | 168 |
| Ni/N-doped porous carbon | ZIF-8 | −0.9 V *vs.* RHE | 0.5 M $KHCO_3$ | $FE_{CO} = 71.9$ | 49 |
| Fe–N-doped porous carbon | ZIF-8 | −0.33 V *vs.* RHE | 1 M $KHCO_3$ | $FE_{CO} = 89.1$ | 194 |
| Co–N-doped porous carbon | Co/Zn ZIF | −0.3 V to −0.9 V *vs.* RHE | 0.5 M $KHCO_3$ | $FE_{CO} = 94$ | 50 |
| N-doped porous carbon | ZIF-8 | −0.93 V *vs.* RHE | 0.1 M $KHCO_3$ | $FE_{CO} = 78$ | 165 |
| Fe–N-doped porous carbon | ZIF-8 | −0.47 V *vs.* RHE | 0.1 M $KHCO_3$ | $FE_{CO} = 93$ | 162 |
| Fe–N-doped porous carbon | ZIF-7 | −0.33 V to −0.83 V *vs.* RHE | 1.0 M $KHCO_3$ | $FE_{CO} = 86$ | 211 |
| Meso N–C–Fe | Fe-ZIF-8@$SiO_2$ | −0.73 V *vs.* RHE | 0.1 M $KHCO_3$ | $FE_{CO} = 85$ | 189 |
| Ni–N–C | Zn–Ni MOF | −0.54 V *vs.* RHE | 0.5 M $KHCO_3$ | $FE_{CO} = 95.1$ | 263 |
| Ni/Fe–N–C | Zn/Ni/Fe ZIF | −0.7 V *vs.* RHE | 0.5 M $KHCO_3$ | $FE_{CO} = 98$ | 201 |
| CuSAs/TCNFs[b] | Cu/ZIF-8 | −0.9 V *vs.* RHE | 0.1 M $KHCO_3$ | $FE_{CH_3OH} = 44$ $FE_{CO} = 56$ | 173 |
| Ni–C–N | Zr-MOF (PCN-222) | −0.30 V *vs.* RHE | 0.5 M $KHCO_3$ | $FE_{CO} = 98.7$ | 202 |
| Cu–N | Cu-MOF | −1.01 V *vs.* RHE | 0.1 M $KHCO_3$ | $FE_{C_2H_2} = 11.2$ $FE_{CH_3CH_2OH} = 18.4$ | 222 |
| Cu–Zn–N–C | Cu/Zn ZIF | Overall potential difference = 1.5 V | 0.5 M $NaHCO_3$ | $FE_{CH_4} = 95.6$ | 223 |
| $Ni_{SA}$–N–C | Mg–Ni-MOF-74 | −0.8 V *vs.* RHE | 0.5 M $KHCO_3$ | $FE_{CO} = 98$ | 157 |
| Fe–, Co–, Ni–, Cu–N–C | Porphyrinic MOF | −0.8 V *vs.* RHE | 0.5 M $KHCO_3$ | $FE_{CO} = 96.8$ | 200 |
| Ni–$N_3$–C | Ni–Zn-MOF | −0.65 V *vs.* RHE | 0.5 M $KHCO_3$ | $FE_{CO} = 95.6$ | 186 |
| Ni–C–N | $NH_2$–Ni-MOF | −0.79 V *vs.* RHE | 0.5 M $KHCO_3$ | $FE_{CO} = 97$ | 224 |
| Fe–Ni–N–C | Fe/ZnO, Ni/ZnO doped ZIF-8 | −0.5 V *vs.* RHE | | $FE_{CO} = 96.2$ | 52 |
| Ni–N–C | ZIF-8@$Ni^{2+}$ | −0.7 V *vs.* RHE | 0.1 M $KHCO_3$ | $FE_{CO} = 98$ | 203 |
| $Mn_{SA}$-SNC[c] | ZIF-8 | −0.45 V *vs.* RHE | 0.5 M $KHCO_3$ | $FE_{CO} = 70$ | 195 |
| Ni nano cluster on N-doped carbon | $NH_2$–Zn/Ni-MOF | −0.88 V *vs.* RHE | 0.5 M $KHCO_3$ | $FE_{CO} = 98.7$ | 226 |
| Oxide derived Cu/C | HKUST-1 | −0.7 V *vs.* RHE | 0.1 M $KHCO_3$ | $FE_{methanol} = 13.8–43.2$ $FE_{ethanol} = 24–34.8$ | 246 |
| Ag/$Co_3O_4$ | Ag/Co-mixed metal MOF | −1.8 V *vs.* SCE | 0.1 M $KHCO_3$ | $FE_{CO} = 55.6$ | 249 |
| Cu NPs clusters | MOF-74 | −1.3 V *vs.* RHE | 0.1 M $KHCO_3$ | $FE_{CH_4} = 50$ | 250 |
| Cu/$Cu_2O$ | Cu-MOF | −0.76 V *vs.* RHE | 0.5 M $KHCO_3$ | $FE_{CO} = 43.8$ | 251 |
| Cu nanoribbons | Cu-MOF | | 1 M KOH | $FE_{C_{2+}} = 82.3$ | 51 |
| In–Cu bimetallic oxides | $In_2O_3$@Cu-MOF | −0.8 V *vs.* RHE | 0.5 M $KHCO_3$ | $FE_{CO} = 92.1$ | 255 |
| $Cu_3P$/C | HKUST | −0.3 V *vs.* RHE | 0.1 M $NaHCO_3$ | $FE_{CO} = 47$ | 256 |
| $Cu_2O$/Cu@N-doped porous carbon | Cu-MOF | −0.68 V *vs.* RHE | 0.1 M $NaHCO_3$ | $FE_{HCOO^-} = 70.5$ | 257 |
| Bi-based nanoparticles | CAU-7[d] | −0.97 *vs.* RHE | 0.5 M $NaHCO_3$ | $FE_{HCOO^-} = 95$ | 260 |

[a] Multiwall carbon nanotubes. [b] Cu single atoms through carbon nanofibers. [c] Mn single-atom-sulfurized-nitrogen-doped carbon. [d] Bi(1,3,5-tris(4-carboxyphenyl)benzene) Bi(btb).

be easily tuned, exactly as in the case of small molecular homogenous systems, which enables the fine-tuning of the active sites and the fundamental understanding of the catalytic mechanism. It is well known that the poor electrical conductivity of bulk MOFs is a serious limitation for their applications not only in $CO_2$RR but in most electrocatalytic applications. However, this issue can be partially solved by constructing highly conductive 2D chains or so-called coordination nanosheets (CONASHs).[264,265] However, this is limited to a particular type of ligand structure. Another approach to mitigate the low electrical conductivity of MOFs is to utilize them as precursors for creating conductive carbonaceous materials that are doped with some transition metals derived from the starting structure. In this case, the original structure collapses and the molecular nature of MOFs does not exist. Thus, mechanistic studies will be more difficult in this case given that we do not know the exact structure of the active sites. This can explain the poor

 This journal is © The Royal Society of Chemistry 2024

Published on 25 August 2024. Downloaded on 02.05.26 08:00:32.

mechanistic investigations related to MOF-based electrocatalysts in $CO_2$RR.

$CO_2$RR has numerous reaction pathways *via* 2-, 4-, 6-, and 8-electron reduction steps, with multiple possible reduction products. The binding strength of the reaction intermediates as *H, *COOH, *OCOH, and *CO (asterisk (*) indicates the adsorbed species) to the catalyst surface is the critical factor that controls the product selectivity.[59,266,267] The binding energy of the catalyst with a particular intermediate may favor the related reaction pathway over other possible paths. Thus, it is necessary to know and accordingly tune the electrocatalyst surface properties to further control their $CO_2$RR performances. The nonselective reduction of $CO_2$ is mainly due to the competition between $H^+$ and $CO_2$ for the key intermediates that produce diverse reduction products through distinct pathways (Table 1). The most common reduction products are carbon monoxide (CO), oxalic acid ($C_2O_4H_2$), formic acid (HCOOH), formaldehyde ($CH_2O$), and methanol ($CH_3OH$). However, the formation of other reduction products such as methane ($CH_4$), ethylene ($CH_2CH_2$), and ethanol ($CH_3CH_2OH$) is becoming feasible, particularly with copper-based electrocatalysts.

Scheme 1 outlines one of the plausible mechanisms for the catalytic reduction of $CO_2$ into $HCO_2^-$ and CO, together with $H^+$ into $H_2$, the most competitive reaction for $CO_2$RR in molecular catalytic systems. Upon the reduction of the transition metal ion, the reduced intermediate can undergo either protonation to form a metal hydride intermediate or directly activate $CO_2$. In the protonation pathway, upon the generation of a metal hydride, it can react either with a second proton to form $H_2$ or with $CO_2$ to produce formate. Conversely, the $CO_2$-activation pathway involves $CO_2$ activation to surpass protonation at the reduced metal center. CO is the specific product; however, in this case, the competition between both pathways is quite complex. For instance, reaching high negative potentials to activate $CO_2$ make the metal sites more Brønsted basic, which favors both pathways, thus negatively affecting the overall selectivity and efficiency of the catalyst. Further, the reaction product, *i.e.*, CO, is often a better ligand than $CO_2$; consequently, enhancing the electron density around the metal center often leads to a more stable M–CO complex, which inhibits the catalyst turnover. Thus, it is clear that for optimal $CO_2$ reduction to CO, an in-depth comprehension of how $CO_2$, CO, and $H^+$ interact with the reduced metal centers is crucial in catalyst design.[268]

In heterogeneous systems, it is generally accepted that $CO_2$RR involves several steps, including $CO_2$-adsorption, intermediate formation, production of reaction products, and desorption of the final products.[269] Accordingly, to understand the $CO_2$RR mechanism for a particular catalytic system, *in situ* characterization techniques, together with theoretical/computational studies, are being widely used. For instance, to gain insights into the superior catalytic activity and excellent selectivity of Co-PMOF (cobalt-based polyoxometalate metalloporphyrin organic frameworks), Wang *et al.* performed thorough DFT calculations. They suggested that $CO_2$ electrochemical reduction to CO includes firstly a proton-coupled electron transfer process to generate a carboxyl intermediate (*COOH), and eventually, for the formation of the *CO intermediate, a second charge transfer (one electron and one proton), followed by CO desorption for the final CO product (Fig. 12a). Based on the calculated free energy diagrams, the RDSs for $CO_2$RR on zinc polyoxometalate (Zn-POM) and Co-TCPP, independently, are the formation of adsorbed intermediates *COOH and *CO with relatively high free energies of $\Delta G_1 = 0.96$ eV and $\Delta G_2 = 0.53$ eV, respectively. However, when Zn-POM and Co-TCPP were assembled into one polymeric structure, the final compound of Co-PMOF possessed considerably reduced free energies, particularly the RDS of *COOH production ($\Delta G_1 = 0.34$ eV), which is consistent with the high activity and selectivity of this bimetallic MOF. Calculations indicated

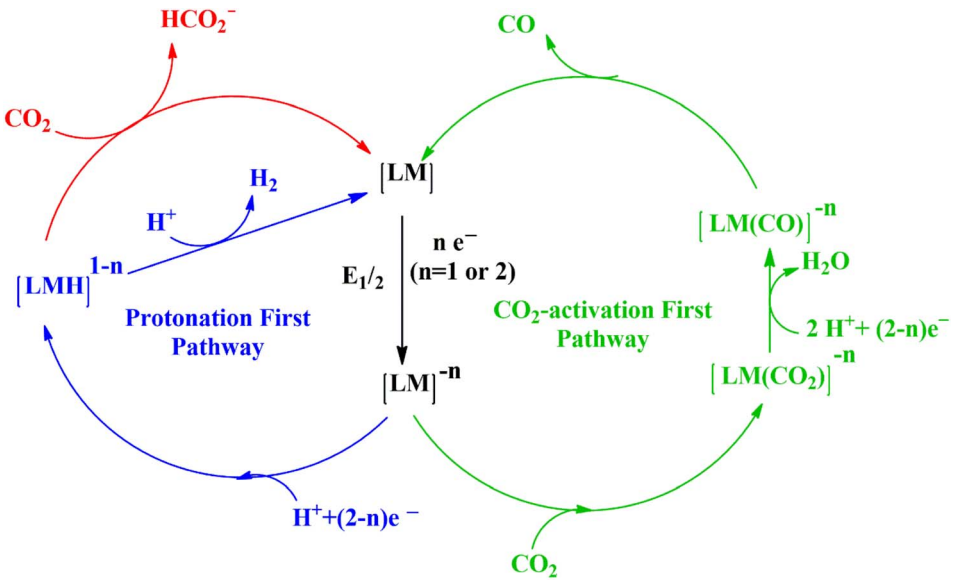


Scheme 1 Generalized scheme for $CO_2$ activation using molecular catalysts (M = metal, L = ligand, and $n$ = charge).[268]

Published on 25 August 2024. Downloaded on 02.05.26 08:00:32.

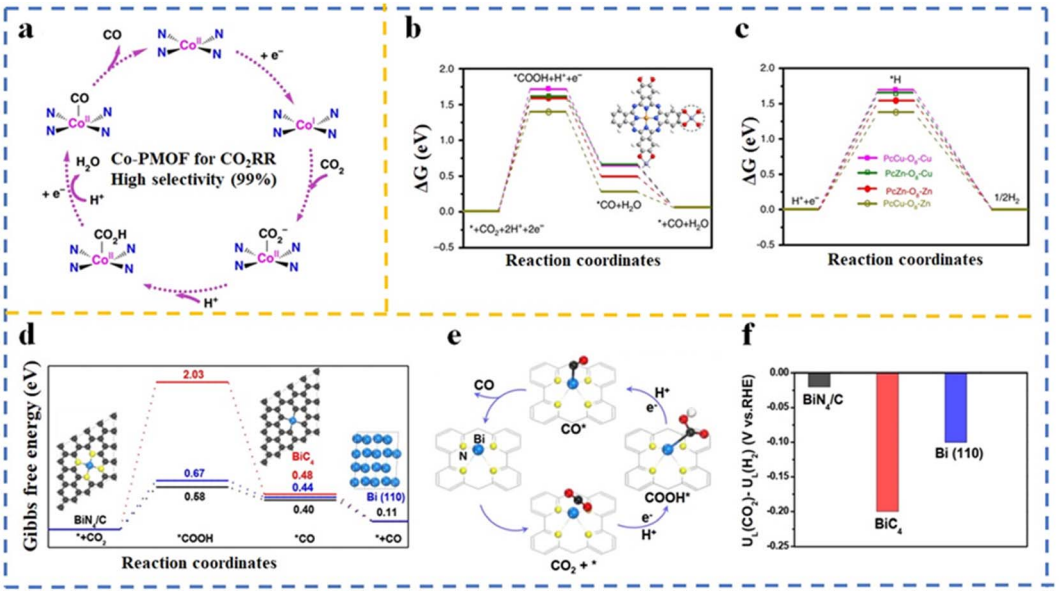


Fig. 12 (a) Suggested reaction pathway for the $CO_2$RR on Co-PMOF. Adopted with permission.[270] Copyright 2018, Nature Publishing Group. (b and c) Gibbs free energy diagram of the $CO_2$RR on $M1O_4$ units in the structure of PCM-$O_8$-$M_1$. Reproduced with permission.[103] Copyright 2020, Nature Publishing Group. (d) Gibbs free energy profile of the $CO_2$RR, (e) proposed mechanism on the $BiN_4$/C surface, (f) difference in the limiting potentials in the reduction of $CO_2$ and $H_2$ evolution. Reproduced with permission.[271] Copyright 2019, the American Chemical Society.

that the Co centers are the favorite sites for $CO_2$ coordination instead of POM, and they also demonstrated the synergistic electron modulation of POM and the porphyrin metal center. It also highlighted that upon the replacement of Co in the porphyrin center with Ni or Zn, the RDS remains the formation of *COOH; however, it has much higher free energies, making its formation more sluggish. In the case of Fe-PMOF, although the energy for the formation of *COOH and *CO decreased as compared to that of Co-PMOF, the desorption of CO becomes more challenging, which can be ascribed to the higher affinity of Fe for the CO ligand.[270] Similarly, DFT calculations for a model system of cobalt phthalocyanine (CoPc), with a metal–$N_4$ coordination structure, showed that by compromising on the crucial reaction steps of *COOH production and *CO desorption, it improves the overall reaction thermodynamics, which is consistent with the experimental results, where it achieved an excellent FE of 99% for $CO_2$RR to CO with a mild potential of −0.8 V *vs.* RHE compared to other metal phthalocyanines (MPcs).[272] The *in situ* spectro-electrochemical characterization of cobalt-metallated [$Al_2(OH)_2$TCPPCo] MOF@FTO-electrode in a $CO_2$-saturated electrolyte revealed the formation of Co(I) species under the operating conditions with a Tafel slope of 165 mV per decade, suggesting that the RDS in this catalytic cycle may be either a $CO_2$ binding to a Co(I) porphyrin coupled with a one-electron reduction or a one-electron reduction of a Co(I)–$CO_2$ adduct. A fraction of Co(II) is reduced to Co(I) even at potentials more positive than −0.4 V *vs.* RHE, which is likely to participate in the catalytic reduction of $CO_2$ to CO.[273]

In an analogous structure, a 2D conjugated MOF (2D *c*-MOF) with metal-phthalocyanine as the linker ($MN_4$) and metal-bis(dihydroxy) complex ($M1O_4$) as the metal node (PcM-$O_8$-M1), DFT calculations revealed that the formation of *COOH *via* protonation is the rate-determining step. Based on the binding energies, it was found that the *COOH intermediate has a more robust interaction. In contrast, *H has a weaker interplay with the linkages ($M1O_4$ complexes) in comparison to that of the phthalocyanine macrocycles. Thus, it was proposed that $CO_2$ activation mainly happens at the $M1O_4$ sites, while the $MN_4$ complex serves as the active site for HER. Further, Gibbs free energy calculations demonstrated that the $ZnO_4$ complex ion of PcCu–$O_8$ has the lowest values for *COOH formation, and also the lowest overpotential compared to other $M1O_4$ structures in PcM-$O_8$-$M_1$ (Fig. 12b), which agreed with the experimental results. In addition, the overpotential for $CO_2$RR at $M1O_4$ was found to be affected by different $MN_4$ complexes in the Pc ligand. Exploring the energy profile for HER on $MN_4$ and $M1O_4$ moieties indicates that the $CuN_4$ moiety in PcCu–$O_8$–Zn has the lowest HER energy barrier and the fastest proton/electron transfer kinetics among the different metal centers (Fig. 12c), suggesting the synergistic effect between the $CuN_4$ and $ZnO_4$ moieties given that the $CuN_4$ complex facilitates the protonation of adsorbed *$CO_2$ on the $ZnO_4$ complexes, and thus accelerates the overall $CO_2$RR kinetics.[274] Similarly, computational studies of $CO_2$RR on the surface of a bimetallic Ni–Fe-based 2D MOF suggested that $CO_2$ is activated on the surface of Ni, Fe, and H atom (from the ligand) with proton/electron pair transfer, allowing the intermediate (*COOH) to bind with the metal atoms *via* a carbon atom. Calculations indicated that Ni-ions are the preferable catalytic sites for $CO_2$RR with a low overpotential of 0.19 V *vs.* RHE, and they can stabilize *COOH more than the Fe-sites, resulting in a low activation barrier. Additionally, the interaction between *CO and Ni-site is weaker than *CO and Fe-site. Finally, the mechanism for the $CO_2$RR to CO over MOF Ni–Fe was proposed. It was proposed that after the

 This journal is © The Royal Society of Chemistry 2024

Published on 25 August 2024. Downloaded on 02.05.26 08:00:32.

adsorption and attachment of $CO_2$ to the surface of the electrode, it captures an electron to form $CO_2^{\bullet-}$, a transitional product, which is known to be the rate-determining step. Afterwards, the $CO_2^{\bullet-}$ intermediate will capture another electron for the adsorbed CO ($CO_{ads}$), which is then desorbed and released into the electrolyte.[275]

MOF-derived materials, particularly metal–N–C, metal–$N_4$ structures, and M-SACs, have also received considerable attention in $CO_2$RR, and interesting findings have been attained. However, the actual active sites and reaction mechanisms still need to be clarified due to the uncertainty about the exact atomic structure of the investigated materials. Although advanced characterization techniques such as X-ray absorption spectroscopy (XAS) can provide substantial information about the atomic structure of different materials, it is not easily available. Bismuth single atoms were obtained *via* the thermal decomposition of a bismuth-based metal–organic framework (Bi-MOF), denoted as Bi–$N_4$ sites on porous carbon networks, which had high intrinsic activity for $CO_2$R to CO with a high FE (FECO up to 97%) and high TOF of 5535 $h^{-1}$ at a low overpotential of 0.39 V *vs.* RHE. In the DFT calculations, $BiN_4$/C $BiC_4$ and Bi (110) were considered to understand the effect of the coordination environment on the free energy of the reaction intermediates. It was found that the formation of the COOH* intermediate *via* $CO_2$ activation is the RDS in all three materials because of the uphill energy barrier for the first proton-coupled electron-transfer step (Fig. 12d–f). $BiN_4$/C had a lower Gibbs free energy for the generation of the *COOH intermediate, matching its better performance and low onset potential. Further, $BiN_4$/C has a more positive $U_L(CO_2) - U_L(H_2)$ value (−0.02 V) than Bi(110) (−0.1 V) and $BiC_4$ (−0.2 V), implying its higher selectivity for $CO_2$ conversion to CO, where $U_L(CO_2) - U_L(H_2)$ refers to the difference between the limiting potentials for $CO_2$ reduction and $H_2$ evolution. It is noteworthy that previous studies suggested that the value of $U_L(CO_2) - U_L(H_2)$ reflects the selectivity of the $CO_2$RR, where a more positive value means a better selectivity for $CO_2$RR over HER.[241]

## 5. Conclusions and outlooks

This review comprehensively explored the recent advancements in the design and application of MOFs and MOF-derived materials for electrochemical $CO_2$ reduction reactions ($CO_2$RR). The discussion highlighted the unique properties of MOFs, such as their porous structures, tunable active sites, and the ability to be converted into highly efficient electrocatalysts through pyrolysis and other treatments. Significant progress has been made in enhancing the stability, conductivity, and catalytic activity of these materials, making them promising candidates for $CO_2$RR.

Pristine MOFs have shown considerable potential in $CO_2$RR due to their well-defined active sites and the ability to modify their microenvironment, which are crucial for optimizing their catalytic activity and selectivity. MOFs containing transition metals such as Cu, Zn, Ni, Zr, Co, and Fe have demonstrated significant activity in $CO_2$RR. Copper-based MOFs are generally inclined towards the production of hydrocarbons (methane), alcohols (ethanol and methanol), and oxalates. Alternatively, Zn-, Ni-, Co-, Zr-, and Fe-based MOFs generally exhibit high selectivity towards CO. However, the poor stability and electrical conductivity and lack of mesoporosity of these pristine MOFs remain a significant challenge, especially in aqueous environments.

Thus, MOF-derived materials present several distinct advantages over pristine MOFs in the context of $CO_2$RR. One of the most significant benefits is their enhanced stability, especially under electrochemical conditions. Although pristine MOFs often suffer from hydrolytic instability and poor electrical conductivity, MOF-derived materials, typically obtained through processes such as pyrolysis, exhibit improved durability and conductivity. These materials retain the advantageous porous structure of the parent MOFs, allowing for high surface areas and accessible active sites, but with the added benefit of increased conductivity due to the formation of conductive carbon frameworks. Additionally, the thermal treatment involved in the conversion of MOFs to MOF-derived materials generally leads to the incorporation of heteroatoms (*e.g.*, nitrogen, oxygen, and sulfur) in the carbon matrix, which can further enhance the catalytic activity and selectivity by modulating the electronic properties of the active sites.

MOF-derived materials exhibit a variety of catalytic behaviours depending on the type of transition metal and the structural modifications applied to the MOF. N-doped porous carbon materials derived from MOFs such as ZIF-8, Zn-MOF-74, and Co/Zn ZIF show high selectivity towards CO production, with their FE reaching up to 100% under the optimal conditions. Bismuth- and copper-derived materials typically favor the production of formate ($HCOO^-$) and hydrocarbons (such as $CH_4$ and $C_2H_2$) as well as oxygenated products (methanol and ethanol), with efficiencies reaching up to 95% for formate in Bi-based catalysts and as high as 82.3% for $C_{2+}$ products in Cu-derived catalysts. Nickel and iron-doped MOF-derived carbons also display strong selectivity towards CO, often exceeding 90% FE. Moreover, multi-metallic and single-atom catalysts (SACs) derived from MOFs further enhance the selectivity and efficiency, with $Ni_{SA}$–N–C achieving an FE of 98% for CO production, and Cu–Zn–N–C exhibiting a remarkable FE of 95.6% for $CH_4$ production. These results underline the versatility of MOF-derived materials in tailoring the product selectivity, where the choice of metal, doping, and structural modification directly influence the catalytic outcomes.

Mechanistically, the coordination environment around the metal centres, such as M–$N_4$ sites, plays a crucial role in determining the reaction pathways and product selectivity. The catalytic performance is often governed by the adsorption and activation of $CO_2$ on the metal sites, followed by proton-coupled electron transfer steps. The presence of dopants or additional heteroatoms (such as N and S) within MOF-derived materials further modulates the electronic environment of the active sites, enhancing their ability to stabilize the reaction intermediates and lower the energy barriers for the rate-limiting steps towards a particular product.

The stability and durability of MOF-based materials under electrochemical conditions, particularly in aqueous

Published on 25 August 2024. Downloaded on 02.05.26 08:00:32.

environments, represent a significant challenge in $CO_2$RR applications. Pristine MOFs often undergo hydrolysis and structural degradation, leading to a decline in their catalytic activity over time, which hinders their practical application. Additionally, the poor electrical conductivity of many MOFs presents another obstacle, given that it limits efficient charge transfer during $CO_2$RR, resulting in substantial ohmic losses and reduced catalytic efficiency. Furthermore, the lack of mesoporosity in MOF materials is a limitation given that mesoporosity facilitates liquid mass transfer. Identifying and controlling the active sites within MOF-derived materials are also complex, especially in systems with multiple potential active sites, which complicates the determination of the specific sites responsible for catalysis. Furthermore, the scalability and cost of synthesizing MOFs and their derivatives pose challenges for their widespread industrial application, necessitating the development of more cost-effective and scalable synthesis methods.

Moving forward, enhancing the stability of MOF-based materials in aqueous and electrochemical environments is a critical focus for future research. This can involve designing MOFs with stronger metal–ligand bonds, incorporating hydrophobic ligands, or developing hybrid materials that combine the advantages of MOFs with more stable substances. To address their conductivity issue, efforts can focus on using conductive coordination nanosheets or 2D MOFs, integrating conductive polymers, carbon-based materials, or metallic nanoparticles into MOF structures. Additionally, using MOFs as precursors for synthesizing metal or metal-heteroatom-doped, highly conductive carbonaceous materials or single-atom catalysts (SACs) can be a promising approach to further expand the research in this direction. Advanced *in situ* and *operando* characterization techniques will be essential in better understanding the active sites and mechanisms involved in $CO_2$RR, helping to guide the rational design of more effective catalysts. Finally, efforts to bridge the gap between laboratory research and industrial application should prioritize the development of catalysts that not only offer high selectivity and efficiency but also demonstrate robustness and scalability in real devices.

## Data availability

No primary research results, software or code has been included and no new data were generated or analysed as part of this review.

## Conflicts of interest

The authors declare no conflict of interest.

## Acknowledgements

D. P. D. thanks the Francqui Foundation for the Francqui Research Professor chair. H. A. Y. and M. A. A acknowledge the support from His Majesty Trust Fund (HMTF), Oman (Project ID: SR/DVC/NRC/24/01).

## Notes and references

1 T. Boden, R. Andres and G. Marland, *Global, Regional, and National Fossil-Fuel $CO_2$ Emissions (1751–2014)*, Environmental System Science Data Infrastructure for a Virtual Ecosystem, 2017.
2 O. Edenhofer, *Climate Change 2014: Mitigation of Climate Change*, Cambridge University Press, 2015.
3 A. J. Morris, G. J. Meyer and E. Fujita, *Acc. Chem. Res.*, 2009, **42**, 1983–1994.
4 H. Takeda and O. Ishitani, *Coord. Chem. Rev.*, 2010, **254**, 346–354.
5 J. L. White, M. F. Baruch, J. E. Pander III, Y. Hu, I. C. Fortmeyer, J. E. Park, T. Zhang, K. Liao, J. Gu and Y. Yan, *Chem. Rev.*, 2015, **115**, 12888–12935.
6 C. I. Ezugwu, S. Liu, C. Li, S. Zhuiykov, S. Roy and F. Verpoort, *Coord. Chem. Rev.*, 2022, **450**, 214245.
7 J. Shi, Y. Jiang, Z. Jiang, X. Wang, X. Wang, S. Zhang, P. Han and C. Yang, *Chem. Soc. Rev.*, 2015, **44**, 5981–6000.
8 A. Taheri Najafabadi, *Int. J. Energy Res.*, 2013, **37**, 485–499.
9 G. Centi, E. A. Quadrelli and S. Perathoner, *Energy Environ. Sci.*, 2013, **6**, 1711–1731.
10 N. Gholampour, Y. Zhao, F. Devred, C. Sassoye, S. Casale and D. P. Debecker, *ChemCatChem*, 2023, **15**, e202201338.
11 J. Durst, A. Rudnev, A. Dutta, Y. Fu, J. Herranz, V. Kaliginedi, A. Kuzume, A. A. Permyakova, Y. Paratcha and P. Broekmann, *Chimia Int J. Chem.*, 2015, **69**, 769–776.
12 J. Albo, M. Alvarez-Guerra, P. Castaño and A. Irabien, *Green Chem.*, 2015, **17**, 2304–2324.
13 J. Qiao, Y. Liu, F. Hong and J. Zhang, *Chem. Soc. Rev.*, 2014, **43**, 631–675.
14 J. P. Jones, G. S. Prakash and G. A. Olah, *Isr. J. Chem.*, 2014, **54**, 1451–1466.
15 R. Kortlever, J. Shen, K. J. P. Schouten, F. Calle-Vallejo and M. T. Koper, *J. Phys. Chem. Lett.*, 2015, **6**, 4073–4082.
16 U. Nwabara, S. Verma, A. A. Gewirth and P. J. Kenis, *ECS Meeting Abstracts*, 2018, **01**(28), 1630.
17 R. J. Lim, M. Xie, M. A. Sk, J.-M. Lee, A. Fisher, X. Wang and K. H. Lim, *Catal. Today*, 2014, **233**, 169–180.
18 M. F. Hasan, L. M. Rossi, D. P. Debecker, K. C. Leonard, Z. Li, B. C. Makhubela, C. Zhao and A. Kleij, *ACS Sustain. Chem. Eng.*, 2021, **9**, 12427–12430.
19 R.-Z. Zhang, B.-Y. Wu, Q. Li, L.-L. Lu, W. Shi and P. Cheng, *Coord. Chem. Rev.*, 2020, **422**, 213436.
20 H. A. Younus, N. Ahmad, W. Ni, X. Wang, M. Al-Abri, Y. Zhang, F. Verpoort and S. Zhang, *Coord. Chem. Rev.*, 2023, **493**, 215318.
21 C. Long, X. Li, J. Guo, Y. Shi, S. Liu and Z. Tang, *Small Methods*, 2019, **3**, 1800369.
22 Y. i. Hori, in *Modern Aspects of Electrochemistry*, Springer, 2008, pp. 89–189.
23 X. Duan, J. Xu, Z. Wei, J. Ma, S. Guo, S. Wang, H. Liu and S. Dou, *Adv. Mater.*, 2017, **29**, 1701784.
24 K. Zhao and X. Quan, *ACS Catal.*, 2021, **11**, 2076–2097.
25 A. Vasileff, Y. Zheng and S. Z. Qiao, *Adv. Energy Mater.*, 2017, **7**, 1700759.

 This journal is © The Royal Society of Chemistry 2024

Published on 25 August 2024. Downloaded on 02.05.26 08:00:32.

26 S. Lin, C. S. Diercks, Y.-B. Zhang, N. Kornienko, E. M. Nichols, Y. Zhao, A. R. Paris, D. Kim, P. Yang and O. M. Yaghi, *Science*, 2015, **349**, 1208–1213.
27 M. Lu, M. Zhang, J. Liu, Y. Chen, J.-P. Liao, M.-Y. Yang, Y.-P. Cai, S.-L. Li and Y.-Q. Lan, *Angew. Chem., Int. Ed.*, 2022, **61**, e202200003.
28 J. Francis Kurisingal, H. Kim, J. Hyeak Choe and C. Seop Hong, *Coord. Chem. Rev.*, 2022, **473**, 214835.
29 P. Shao, L. Yi, S. Chen, T. Zhou and J. Zhang, *J. Energy Chem.*, 2020, **40**, 156–170.
30 X. Li and Q.-L. Zhu, *EnergyChem*, 2020, **2**, 100033.
31 S. Gulati, S. Vijayan, S. Kumar, B. Harikumar, M. Trivedi and R. S. Varma, *Coord. Chem. Rev.*, 2023, **474**, 214853.
32 X. Li and Q.-L. Zhu, *EnergyChem*, 2020, **2**, 100033.
33 L. Valenzuela, G. Amariei, C. I. Ezugwu, M. Faraldos, A. Bahamonde, M. E. Mosquera and R. Rosal, *Sep. Purif. Technol.*, 2022, **285**, 120351.
34 C. I. Ezugwu, S. Ghosh, M. E. Mosquera and R. Rosal, in *Nanomaterials for Water Treatment and Remediation*, CRC Press, 2021, pp. 371–408.
35 D. Skoda, T. Kazda, L. Munster, B. Hanulikova, A. Styskalik, P. Eloy, D. P. Debecker, P. Vyroubal, L. Simonikova and I. Kuritka, *J. Mater. Sci.*, 2019, **54**, 14102–14122.
36 O. Shekhah, J. Liu, R. Fischer and C. Wöll, *Chem. Soc. Rev.*, 2011, **40**, 1081–1106.
37 N. Gholampour, C. I. Ezugwu, S. Rahmdele, A. G. Gilanie and F. Verpoort, *Resour. Chem. Mater.*, 2022, **1**(3–4), 201–210.
38 C. I. Ezugwu, J. M. Sonawane and R. Rosal, *Sep. Purif. Technol.*, 2021, 120246.
39 A. H. Chughtai, N. Ahmad, H. A. Younus, A. Laypkov and F. Verpoort, *Chem. Soc. Rev.*, 2015, **44**, 6804–6849.
40 V. Remya and M. Kurian, *Int. Nano Lett.*, 2019, **9**, 17–29.
41 M. Safaei, M. M. Foroughi, N. Ebrahimpoor, S. Jahani, A. Omidi and M. Khatami, *TrAC, Trends Anal. Chem.*, 2019, **118**, 401–425.
42 M.-R. Ahmadian-Yazdi, N. Gholampour and M. Eslamian, *ACS Appl. Energy Mater.*, 2020, **3**, 3134–3143.
43 M. Hao, M. Qiu, H. Yang, B. Hu and X. Wang, *Sci. Total Environ.*, 2021, **760**, 143333.
44 B. Zhang, J. Zhang, M. Hua, Q. Wan, Z. Su, X. Tan, L. Liu, F. Zhang, G. Chen and D. Tan, *J. Am. Chem. Soc.*, 2020, **142**, 13606–13613.
45 Q. Huang, Q. Li, J. Liu, R. Wang and Y.-Q. Lan, *Matter*, 2019, **1**, 1656–1668.
46 J.-X. Wu, S.-Z. Hou, X.-D. Zhang, M. Xu, H.-F. Yang, P.-S. Cao and Z.-Y. Gu, *Chem. Sci.*, 2019, **10**, 2199–2205.
47 N. Kornienko, Y. Zhao, C. S. Kley, C. Zhu, D. Kim, S. Lin, C. J. Chang, O. M. Yaghi and P. Yang, *J. Am. Chem. Soc.*, 2015, **137**, 14129–14135.
48 L. Ye, Y. Ying, D. Sun, Z. Zhang, L. Fei, Z. Wen, J. Qiao and H. Huang, *Angew. Chem., Int. Ed.*, 2020, **59**, 3244–3251.
49 C. Zhao, X. Dai, T. Yao, W. Chen, X. Wang, J. Wang, J. Yang, S. Wei, Y. Wu and Y. Li, *J. Am. Chem. Soc.*, 2017, **139**, 8078–8081.
50 X. Wang, Z. Chen, X. Zhao, T. Yao, W. Chen, R. You, C. Zhao, G. Wu, J. Wang and W. Huang, *Angew. Chem., Int. Ed.*, 2018, **57**, 1944–1948.
51 H. Huo, J. Wang, Q. Fan, Y. Hu and J. Yang, *Adv. Energy Mater.*, 2021, **11**, 2102447.
52 L. Jiao, J. Zhu, Y. Zhang, W. Yang, S. Zhou, A. Li, C. Xie, X. Zheng, W. Zhou and S.-H. Yu, *J. Am. Chem. Soc.*, 2021, **143**, 19417–19424.
53 V. K. Abdelkader-Fernandez, D. M. Fernandes and C. Freire, *J. $CO_2$ Util.*, 2020, **42**, 101350.
54 Y. Zhao, L. Zheng, D. Jiang, W. Xia, X. Xu, Y. Yamauchi, J. Ge and J. Tang, *Small*, 2021, **17**, 2006590.
55 S. S. A. Shah, T. Najam, M. Wen, S.-Q. Zang, A. Waseem and H.-L. Jiang, *Small Struct.*, 2022, **3**, 2100090.
56 K. Schouten, Y. Kwon, C. Van der Ham, Z. Qin and M. Koper, *Chem. Sci.*, 2011, **2**, 1902–1909.
57 X. Chang, T. Wang and J. Gong, *Energy Environ. Sci.*, 2016, **9**, 2177–2196.
58 Y. Hori, K. Kikuchi and S. Suzuki, *Chem. Lett.*, 1985, **14**, 1695–1698.
59 A. A. Peterson, F. Abild-Pedersen, F. Studt, J. Rossmeisl and J. K. Nørskov, *Energy Environ. Sci.*, 2010, **3**, 1311–1315.
60 C. S. Diercks, Y. Liu, K. E. Cordova and O. M. Yaghi, *Nat. Mater.*, 2018, **17**, 301–307.
61 F. Song, M. M. Busch, B. Lassalle-Kaiser, C.-S. Hsu, E. Petkucheva, M. l. Bensimon, H. M. Chen, C. Corminboeuf and X. Hu, *ACS Cent. Sci.*, 2019, **5**, 558–568.
62 B. A. Rosen, A. Salehi-Khojin, M. R. Thorson, W. Zhu, D. T. Whipple, P. J. Kenis and R. I. Masel, *Science*, 2011, **334**, 643–644.
63 L. Sun, G. K. Ramesha, P. V. Kamat and J. F. Brennecke, *Langmuir*, 2014, **30**, 6302–6308.
64 S. Kaneco, K. Iiba, H. Katsumata, T. Suzuki and K. Ohta, *Electrochim. Acta*, 2006, **51**, 4880–4885.
65 M. Moura de Salles Pupo and R. Kortlever, *ChemPhysChem*, 2019, **20**, 2926–2935.
66 A. S. Varela, M. Kroschel, T. Reier and P. Strasser, *Catal. Today*, 2016, **260**, 8–13.
67 S. Ma, M. Sadakiyo, R. Luo, M. Heima, M. Yamauchi and P. J. Kenis, *J. Power Sources*, 2016, **301**, 219–228.
68 C.-T. Dinh, T. Burdyny, M. G. Kibria, A. Seifitokaldani, C. M. Gabardo, F. P. García de Arquer, A. Kiani, J. P. Edwards, P. De Luna and O. S. Bushuyev, *Science*, 2018, **360**, 783–787.
69 A. Murata and Y. Hori, *Bull. Chem. Soc. Jpn.*, 1991, **64**, 123–127.
70 R. M. Arán-Ais, D. Gao and B. Roldan Cuenya, *Acc. Chem. Res.*, 2018, **51**, 2906–2917.
71 M. C. Figueiredo, I. Ledezma-Yanez and M. T. M. Koper, *ACS Catal.*, 2016, **6**, 2382–2392.
72 B. Deng, M. Huang, X. Zhao, S. Mou and F. Dong, *ACS Catal.*, 2022, **12**, 331–362.
73 L.-C. Weng, A. T. Bell and A. Z. Weber, *Energy Environ. Sci.*, 2019, **12**, 1950–1968.
74 D. Higgins, C. Hahn, C. Xiang, T. F. Jaramillo and A. Z. Weber, *ACS Energy Lett.*, 2018, **4**, 317–324.

Published on 25 August 2024. Downloaded on 02.05.26 08:00:32.

75 D. M. Weekes, D. A. Salvatore, A. Reyes, A. Huang and C. P. Berlinguette, *Acc. Chem. Res.*, 2018, **51**, 910–918.
76 C.-T. Dinh, T. Burdyny, M. G. Kibria, A. Seifitokaldani, C. M. Gabardo, F. P. García de Arquer, A. Kiani, J. P. Edwards, P. De Luna, O. S. Bushuyev, C. Zou, R. Quintero-Bermudez, Y. Pang, D. Sinton and E. H. Sargent, *Science*, 2018, **360**, 783–787.
77 D. Wakerley, S. Lamaison, J. Wicks, A. Clemens, J. Feaster, D. Corral, S. A. Jaffer, A. Sarkar, M. Fontecave and E. B. Duoss, *Nat. Energy*, 2022, **7**, 130–143.
78 E. W. Lees, B. A. Mowbray, F. G. Parlane and C. P. Berlinguette, *Nat. Rev. Mater.*, 2022, **7**, 55–64.
79 L. Ge, H. Rabiee, M. Li, S. Subramanian, Y. Zheng, J. H. Lee, T. Burdyny and H. Wang, *Chem*, 2022, **8**, 663–692.
80 L. Li, X. Zhang, C. Liu, V. S. S. Mosali, J. Chen, A. M. Bond, Q. Gu and J. Zhang, *Appl. Catal., B*, 2023, **331**, 122597.
81 C.-T. Dinh, F. P. García de Arquer, D. Sinton and E. H. Sargent, *ACS Energy Lett.*, 2018, **3**, 2835–2840.
82 Y. C. Tan, K. B. Lee, H. Song and J. Oh, *Joule*, 2020, **4**, 1104–1120.
83 A. Al Harthi, M. A. Abri, H. A. Younus and R. A. Hajri, *J. $CO_2$ Utiliz.*, 2024, **83**, 102819.
84 J. Y. Zhao, K. Huang, C. Liu, X. Wu, Y. N. Xu, J. Li, M. Zhu, S. Dai, C. Lian and P. F. Liu, *Adv. Funct. Mater.*, 2024, 2316167.
85 X. Yu, Y. Xu, L. Li, M. Zhang, W. Qin, F. Che and M. Zhong, *Nat. Commun.*, 2024, **15**, 1711.
86 T. Liu, K. Ohashi, K. Nagita, T. Harada, S. Nakanishi and K. Kamiya, *Small*, 2022, **18**, 2205323.
87 S. Yan, C. Peng, C. Yang, Y. Chen, J. Zhang, A. Guan, X. Lv, H. Wang, Z. Wang, T.-K. Sham, Q. Han and G. Zheng, *Angew. Chem., Int. Ed.*, 2021, **60**, 25741–25745.
88 R. Senthil Kumar, S. Senthil Kumar and M. Anbu Kulandainathan, *Electrochem. Commun.*, 2012, **25**, 70–73.
89 R. Hinogami, S. Yotsuhashi, M. Deguchi, Y. Zenitani, H. Hashiba and Y. Yamada, *ECS Electrochem. Lett.*, 2012, **1**, H17–H19.
90 X. Kang, Q. Zhu, X. Sun, J. Hu, J. Zhang, Z. Liu and B. Han, *Chem. Sci.*, 2016, **7**, 266–273.
91 M. Jouny, W. Luc and F. Jiao, *Ind. Eng. Chem. Res.*, 2018, **57**, 2165–2177.
92 M. B. Ross, C. T. Dinh, Y. Li, D. Kim, P. De Luna, E. H. Sargent and P. Yang, *J. Am. Chem. Soc.*, 2017, **139**, 9359–9363.
93 F. Li, L. Chen, G. P. Knowles, D. R. MacFarlane and J. Zhang, *Angew. Chem., Int. Ed.*, 2017, **56**, 505–509.
94 X. Jiang, H. Li, J. Xiao, D. Gao, R. Si, F. Yang, Y. Li, G. Wang and X. Bao, *Nano Energy*, 2018, **52**, 345–350.
95 J.-X. Wu, W.-W. Yuan, M. Xu and Z.-Y. Gu, *Chem. Commun.*, 2019, **55**, 11634–11637.
96 S. Dou, J. Song, S. Xi, Y. Du, J. Wang, Z. F. Huang, Z. J. Xu and X. Wang, *Angew. Chem., Int. Ed.*, 2019, **58**, 4041–4045.
97 I. Hod, M. D. Sampson, P. Deria, C. P. Kubiak, O. K. Farha and J. T. Hupp, *ACS Catal.*, 2015, **5**, 6302–6309.
98 X. D. Zhang, S. Z. Hou, J. X. Wu and Z. Y. Gu, *Chemistry*, 2020, **26**, 1604–1611.
99 B.-X. Dong, S.-L. Qian, F.-Y. Bu, Y.-C. Wu, L.-G. Feng, Y.-L. Teng, W.-L. Liu and Z.-W. Li, *ACS Appl. Energy Mater.*, 2018, **1**, 4662–4669.
100 Y.-R. Wang, Q. Huang, C.-T. He, Y. Chen, J. Liu, F.-C. Shen and Y.-Q. Lan, *Nat. Commun.*, 2018, **9**, 1–8.
101 Y. T. Guntern, J. R. Pankhurst, J. Vavra, M. Mensi, V. Mantella, P. Schouwink and R. Buonsanti, *Angew. Chem., Int. Ed.*, 2019, **58**, 12632–12639.
102 R. Matheu, E. Gutierrez-Puebla, M. Á. Monge, C. S. Diercks, J. Kang, M. S. Prévot, X. Pei, N. Hanikel, B. Zhang and P. Yang, *J. Am. Chem. Soc.*, 2019, **141**, 17081–17085.
103 H. Zhong, M. Ghorbani-Asl, K. H. Ly, J. Zhang, J. Ge, M. Wang, Z. Liao, D. Makarov, E. Zschech and E. Brunner, *Nat. Commun.*, 2020, **11**, 1–10.
104 Z. Weng, Y. Wu, M. Wang, J. Jiang, K. Yang, S. Huo, X. F. Wang, Q. Ma, G. W. Brudvig, V. S. Batista, Y. Liang, Z. Feng and H. Wang, *Nat. Commun.*, 2018, **9**, 415.
105 I. Bhugun, D. Lexa and J.-M. Savéant, *J. Am. Chem. Soc.*, 1996, **118**, 1769–1776.
106 D. Yang, Q. Zhu, X. Sun, C. Chen, L. Lu, W. Guo, Z. Liu and B. Han, *Green Chem.*, 2018, **20**, 3705–3710.
107 W. Luc, C. Collins, S. Wang, H. Xin, K. He, Y. Kang and F. Jiao, *J. Am. Chem. Soc.*, 2017, **139**, 1885–1893.
108 F. Sastre, A. V. Puga, L. Liu, A. Corma and H. Garcia, *J. Am. Chem. Soc.*, 2014, **136**, 6798–6801.
109 Y. L. Qiu, H. X. Zhong, T. T. Zhang, W. B. Xu, P. P. Su, X. F. Li and H. M. Zhang, *ACS Appl. Mater. Interfaces*, 2018, **10**, 2480–2489.
110 M. Le, M. Ren, Z. Zhang, P. T. Sprunger, R. L. Kurtz and J. C. Flake, *J. Electrochem. Soc.*, 2011, **158**, E45.
111 K. P. Kuhl, E. R. Cave, D. N. Abram and T. F. Jaramillo, *Energy Environ. Sci.*, 2012, **5**, 7050–7059.
112 M. Perfecto-Irigaray, J. Albo, G. Beobide, O. Castillo, A. Irabien and S. Pérez-Yáñez, *RSC Adv.*, 2018, **8**, 21092–21099.
113 J. Albo, M. Perfecto-Irigaray, G. Beobide and A. Irabien, *J. $CO_2$ Util.*, 2019, **33**, 157–165.
114 J. Albo, D. Vallejo, G. Beobide, O. Castillo, P. Castano and A. Irabien, *ChemSusChem*, 2017, **10**, 1100–1109.
115 M. Perfecto-Irigaray, J. Albo, G. Beobide, O. Castillo, A. Irabien and S. Pérez-Yáñez, *RSC Adv.*, 2018, **8**, 21092–21099.
116 Y. Zhang, Q. Zhou, Z. F. Qiu, X. Y. Zhang, J. Q. Chen, Y. Zhao, F. Gong and W. Y. Sun, *Adv. Funct. Mater.*, 2022, **32**, 2203677.
117 C.-W. Kung, C. O. Audu, A. W. Peters, H. Noh, O. K. Farha and J. T. Hupp, *ACS Energy Lett.*, 2017, **2**, 2394–2401.
118 L. Ye, J. Liu, Y. Gao, C. Gong, M. Addicoat, T. Heine, C. Wöll and L. Sun, *J. Mater. Chem. A*, 2016, **4**, 15320–15326.
119 Z. Weng, Y. Wu, M. Wang, J. Jiang, K. Yang, S. Huo, X.-F. Wang, Q. Ma, G. W. Brudvig and V. S. Batista, *Nat. Commun.*, 2018, **9**, 1–9.
120 J. H. Cho, C. Lee, S. H. Hong, H. Y. Jang, S. Back, M. g. Seo, M. Lee, H. K. Min, Y. Choi and Y. J. Jang, *Adv. Mater.*, 2023, **35**, 2208224.

 This journal is © The Royal Society of Chemistry 2024

Published on 25 August 2024. Downloaded on 02.05.26 08:00:32.

121 C. Li, Y. Ji, Y. Wang, C. Liu, Z. Chen, J. Tang, Y. Hong, X. Li, T. Zheng, Q. Jiang and C. Xia, *Nano–Micro Lett.*, 2023, **15**, 113.
122 Z. Meng, J. Luo, W. Li and K. A. Mirica, *J. Am. Chem. Soc.*, 2020, **142**, 21656–21669.
123 P. Shao, W. Zhou, Q.-L. Hong, L. Yi, L. Zheng, W. Wang, H.-X. Zhang, H. Zhang and J. Zhang, *Angew. Chem., Int. Ed.*, 2021, **60**, 16687–16692.
124 Z.-H. Zhao, H.-L. Zhu, J.-R. Huang, P.-Q. Liao and X.-M. Chen, *ACS Catal.*, 2022, **12**, 7986–7993.
125 Y. Zhang, Q. Zhou, Z.-F. Qiu, X.-Y. Zhang, J.-Q. Chen, Y. Zhao, F. Gong and W.-Y. Sun, *Adv. Funct. Mater.*, 2022, **32**, 2203677.
126 S. Mukhopadhyay, M. S. Naeem, G. Shiva Shanker, A. Ghatak, A. R. Kottaichamy, R. Shimoni, L. Avram, I. Liberman, R. Balilty, R. Ifraemov, I. Rozenberg, M. Shalom, N. López and I. Hod, *Nat. Commun.*, 2024, **15**, 3397.
127 N. C. Burtch, H. Jasuja and K. S. Walton, *Chem. Rev.*, 2014, **114**, 10575–10612.
128 M. Ding, X. Cai and H.-L. Jiang, *Chem. Sci.*, 2019, **10**, 10209–10230.
129 J. Duan, W. Jin and S. Kitagawa, *Coord. Chem. Rev.*, 2017, **332**, 48–74.
130 M. Jahan, Q. Bao and K. P. Loh, *J. Am. Chem. Soc.*, 2012, **134**, 6707–6713.
131 S. Yuan, L. Feng, K. Wang, J. Pang, M. Bosch, C. Lollar, Y. Sun, J. Qin, X. Yang and P. Zhang, *Adv. Mater.*, 2018, **30**, 1704303.
132 D. Narváez-Celada and A. S. Varela, *J. Mater. Chem. A*, 2022, **10**, 5899–5917.
133 S. Dou, J. Song, S. Xi, Y. Du, J. Wang, Z. F. Huang, Z. J. Xu and X. Wang, *Angew. Chem., Int. Ed.*, 2019, **58**, 4041–4045.
134 Y. Wang, P. Hou, Z. Wang and P. Kang, *ChemPhysChem*, 2017, **18**, 3142–3147.
135 L. L. Zhuo, P. Chen, K. Zheng, X. W. Zhang, J. X. Wu, D. Y. Lin, S. Y. Liu, Z. S. Wang, J. Y. Liu and D. D. Zhou, *Angew. Chem., Int. Ed.*, 2022, **61**, e202204967.
136 J. Liu, D. Yang, Y. Zhou, G. Zhang, G. Xing, Y. Liu, Y. Ma, O. Terasaki, S. Yang and L. Chen, *Angew. Chem., Int. Ed.*, 2021, **60**, 14473–14479.
137 Y. Liu, S. Li, L. Dai, J. Li, J. Lv, Z. Zhu, A. Yin, P. Li and B. Wang, *Angew. Chem., Int. Ed.*, 2021, **60**, 16409–16415.
138 X.-F. Qiu, H.-L. Zhu, J.-R. Huang, P.-Q. Liao and X.-M. Chen, *J. Am. Chem. Soc.*, 2021, **143**, 7242–7246.
139 Y. Zhou, S. Chen, S. Xi, Z. Wang, P. Deng, F. Yang, Y. Han, Y. Pang and B. Y. Xia, *Cell Rep. Phys. Sci.*, 2020, **1**(9), 100182.
140 H. Zhong, M. Ghorbani-Asl, K. H. Ly, J. Zhang, J. Ge, M. Wang, Z. Liao, D. Makarov, E. Zschech and E. Brunner, *Nat. Commun.*, 2020, **11**, 1409.
141 H. Zhong, M. Wang, G. Chen, R. Dong and X. Feng, *ACS Nano*, 2022, **16**, 1759–1780.
142 Y.-H. Xiao, Y.-X. Zhang, R. Zhai, Z.-G. Gu and J. Zhang, *Sci. China Mater.*, 2022, **65**, 1269–1275.
143 F. Yang, A. Chen, P. L. Deng, Y. Zhou, Z. Shahid, H. Liu and B. Y. Xia, *Chem. Sci.*, 2019, **10**, 7975–7981.
144 D.-H. Nam, O. S. Bushuyev, J. Li, P. De Luna, A. Seifitokaldani, C.-T. Dinh, F. P. García de Arquer, Y. Wang, Z. Liang, A. H. Proppe, C. S. Tan, P. Todorović, O. Shekhah, C. M. Gabardo, J. W. Jo, J. Choi, M.-J. Choi, S.-W. Baek, J. Kim, D. Sinton, S. O. Kelley, M. Eddaoudi and E. H. Sargent, *J. Am. Chem. Soc.*, 2018, **140**, 11378–11386.
145 J.-D. Yi, R. Xie, Z.-L. Xie, G.-L. Chai, T.-F. Liu, R.-P. Chen, Y.-B. Huang and R. Cao, *Angew. Chem., Int. Ed.*, 2020, **59**, 23641–23648.
146 X. Cao, D. Tan, B. Wulan, K. S. Hui, K. N. Hui and J. Zhang, *Small Methods*, 2021, **5**, 2100700.
147 Z. Chen and Y. Wang, *Fundam. Res.*, 2023, DOI: **10.1016/j.fmre.2023.03.019**.
148 A. Wuttig, C. Liu, Q. Peng, M. Yaguchi, C. H. Hendon, K. Motobayashi, S. Ye, M. Osawa and Y. Surendranath, *ACS Cent. Sci.*, 2016, **2**, 522–528.
149 Y. Gong and T. He, *Small Methods*, 2023, **7**, 2300702.
150 Y. Yang, Y. Yang, Y. Liu, S. Zhao and Z. Tang, *Small Sci.*, 2021, **1**, 2100015.
151 Y. Shen, Y. Zhou, D. Wang, X. Wu, J. Li and J. Xi, *Adv. Energy Mater.*, 2018, **8**, 1701759.
152 W. Chen, B. Han, C. Tian, X. Liu, S. Liang, H. Deng and Z. Lin, *Appl. Catal., B*, 2019, **244**, 996–1003.
153 D. Yu, L. Ge, B. Wu, L. Wu, H. Wang and T. Xu, *J. Mater. Chem. A*, 2015, **3**, 16688–16694.
154 C. Wang, Y. V. Kaneti, Y. Bando, J. Lin, C. Liu, J. Li and Y. Yamauchi, *Mater. Horiz.*, 2018, **5**, 394–407.
155 N. Zaman, N. Iqbal and T. Noor, *Arabian J. Chem.*, 2022, 103906.
156 R. Zhang, L. Jiao, W. Yang, G. Wan and H.-L. Jiang, *J. Mater. Chem. A*, 2019, **7**, 26371–26377.
157 Y. N. Gong, L. Jiao, Y. Qian, C. Y. Pan, L. Zheng, X. Cai, B. Liu, S. H. Yu and H. L. Jiang, *Angew Chem. Int. Ed. Engl.*, 2020, **59**, 2705–2709.
158 L. Jiao, G. Wan, R. Zhang, H. Zhou, S. H. Yu and H. L. Jiang, *Angew. Chem., Int. Ed.*, 2018, **57**, 8525–8529.
159 M. Ma, B. J. Trześniewski, J. Xie and W. A. Smith, *Angew. Chem., Int. Ed.*, 2016, **55**, 9748–9752.
160 S. Back, J.-H. Kim, Y.-T. Kim and Y. Jung, *ACS Appl. Mater. Interfaces*, 2016, **8**, 23022–23027.
161 A. S. Varela, W. Ju and P. Strasser, *Adv. Energy Mater.*, 2018, **8**, 1703614.
162 F. Pan, H. Zhang, K. Liu, D. Cullen, K. More, M. Wang, Z. Feng, G. Wang, G. Wu and Y. Li, *ACS Catal.*, 2018, **8**, 3116–3122.
163 T. N. Huan, N. Ranjbar, G. Rousse, M. Sougrati, A. Zitolo, V. Mougel, F. Jaouen and M. Fontecave, *ACS Catal.*, 2017, **7**, 1520–1525.
164 H. Furukawa, K. E. Cordova, M. O'Keeffe and O. M. Yaghi, *Science*, 2013, **341**, 1230444.
165 R. Wang, X. Sun, S. Ould-Chikh, D. Osadchii, F. Bai, F. Kapteijn and J. Gascon, *ACS Appl. Mater. Interfaces*, 2018, **10**, 14751–14758.
166 Y. Guo, H. Yang, X. Zhou, K. Liu, C. Zhang, Z. Zhou, C. Wang and W. Lin, *J. Mater. Chem. A*, 2017, **5**, 24867–24873.

Published on 25 August 2024. Downloaded on 02.05.26 08:00:32.

167 D. Zhang, Z. Tao, F. Feng, B. He, W. Zhou, J. Sun, J. Xu, Q. Wang and L. Zhao, *Electrochim. Acta*, 2020, **334**, 135563.
168 Q. Zhu, D. Yang, H. Liu, X. Sun, C. Chen, J. Bi, J. Liu, H. Wu and B. Han, *Angew Chem. Int. Ed. Engl.*, 2020, **59**(23), 8896–8901.
169 I. Hod, W. Bury, D. M. Karlin, P. Deria, C. W. Kung, M. J. Katz, M. So, B. Klahr, D. Jin and Y. W. Chung, *Adv. Mater.*, 2014, **26**, 6295–6300.
170 C. Reller, R. Krause, E. Volkova, B. Schmid, S. Neubauer, A. Rucki, M. Schuster and G. Schmid, *Adv. Energy Mater.*, 2017, **7**, 1602114.
171 S. Alizadeh and D. Nematollahi, *J. Am. Chem. Soc.*, 2017, **139**, 4753–4761.
172 J. Li, S. Chen, N. Yang, M. Deng, S. Ibraheem, J. Deng, J. Li, L. Li and Z. Wei, *Angew. Chem., Int. Ed.*, 2019, **58**, 7035–7039.
173 H. Yang, Y. Wu, G. Li, Q. Lin, Q. Hu, Q. Zhang, J. Liu and C. He, *J. Am. Chem. Soc.*, 2019, **141**, 12717–12723.
174 Y. Ren, J. Wang, M. Zhang, Y. Wang, Y. Cao, D. H. Kim and Z. Lin, *Angew. Chem., Int. Ed.*, 2024, **63**, e202315003.
175 J. Li, C. Chen, L. Xu, Y. Zhang, W. Wei, E. Zhao, Y. Wu and C. Chen, *JACS Au*, 2023, **3**, 736–755.
176 Q. Zhang and J. Guan, *Adv. Funct. Mater.*, 2020, **30**, 2000768.
177 Y. Li, S. Wang, X.-s. Wang, Y. He, Q. Wang, Y. Li, M. Li, G. Yang, J. Yi, H. Lin, D. Huang, L. Li, H. Chen and J. Ye, *J. Am. Chem. Soc.*, 2020, **142**, 19259–19267.
178 H. B. Yang, S.-F. Hung, S. Liu, K. Yuan, S. Miao, L. Zhang, X. Huang, H.-Y. Wang, W. Cai and R. Chen, *Nat. Energy*, 2018, **3**, 140–147.
179 E. Luo, H. Zhang, X. Wang, L. Gao, L. Gong, T. Zhao, Z. Jin, J. Ge, Z. Jiang and C. Liu, *Angew. Chem., Int. Ed.*, 2019, **58**, 12469–12475.
180 H. Huang, K. Shen, F. Chen and Y. Li, *ACS Catal.*, 2020, **10**, 6579–6586.
181 H. Zhang, S. Hwang, M. Wang, Z. Feng, S. Karakalos, L. Luo, Z. Qiao, X. Xie, C. Wang and D. Su, *J. Am. Chem. Soc.*, 2017, **139**, 14143–14149.
182 P. Lu, Y. Yang, J. Yao, M. Wang, S. Dipazir, M. Yuan, J. Zhang, X. Wang, Z. Xie and G. Zhang, *Appl. Catal., B*, 2019, **241**, 113–119.
183 T. He, S. Chen, B. Ni, Y. Gong, Z. Wu, L. Song, L. Gu, W. Hu and X. Wang, *Angew. Chem., Int. Ed.*, 2018, **57**, 3493–3498.
184 Q. Zuo, T. Liu, C. Chen, Y. Ji, X. Gong, Y. Mai and Y. Zhou, *Angew. Chem., Int. Ed.*, 2019, **58**, 10198–10203.
185 Y. Zhang, L. Jiao, W. Yang, C. Xie and H.-L. Jiang, *Angew. Chem., Int. Ed.*, 2021, **60**, 7607–7611.
186 Y. Zhang, L. Jiao, W. Yang, C. Xie and H. L. Jiang, *Angew. Chem., Int. Ed.*, 2021, **60**, 7607–7611.
187 L. Fan, P. F. Liu, X. Yan, L. Gu, Z. Z. Yang, H. G. Yang, S. Qiu and X. Yao, *Nat. Commun.*, 2016, **7**, 1–7.
188 H. J. Qiu, Y. Ito, W. Cong, Y. Tan, P. Liu, A. Hirata, T. Fujita, Z. Tang and M. Chen, *Angew. Chem., Int. Ed.*, 2015, **54**, 14031–14035.
189 X. Sun, R. Wang, S. Ould-Chikh, D. Osadchii, G. Li, A. Aguilar, J.-l. Hazemann, F. Kapteijn and J. Gascon, *J. Catal.*, 2019, **378**, 320–330.
190 L. Zhang, Z. Su, F. Jiang, L. Yang, J. Qian, Y. Zhou, W. Li and M. Hong, *Nanoscale*, 2014, **6**, 6590–6602.
191 N. L. Torad, M. Hu, Y. Kamachi, K. Takai, M. Imura, M. Naito and Y. Yamauchi, *Chem. Commun.*, 2013, **49**, 2521–2523.
192 F. Yang, P. Song, X. Liu, B. Mei, W. Xing, Z. Jiang, L. Gu and W. Xu, *Angew. Chem., Int. Ed.*, 2018, **57**, 12303–12307.
193 Z. Chen, K. Mou, S. Yao and L. Liu, *ChemSusChem*, 2018, **11**, 2944–2952.
194 Y. Ye, F. Cai, H. Li, H. Wu, G. Wang, Y. Li, S. Miao, S. Xie, R. Si, J. Wang and X. Bao, *Nano Energy*, 2017, **38**, 281–289.
195 H.-Y. Tan, S.-C. Lin, J. Wang, C.-J. Chang, S.-C. Haw, K.-H. Lin, L. D. Tsai, H.-C. Chen and H. M. Chen, *ACS Appl. Mater. Interfaces*, 2021, **13**, 52134–52143.
196 A. S. Varela, N. Ranjbar Sahraie, J. Steinberg, W. Ju, H. S. Oh and P. Strasser, *Angew. Chem., Int. Ed.*, 2015, **54**(37), 10758–10762.
197 K. Liu, G. Wu and G. Wang, *J. Phys. Chem. C*, 2017, **121**, 11319–11324.
198 M. Lefèvre, E. Proietti, F. Jaouen and J.-P. Dodelet, *Science*, 2009, **324**, 71–74.
199 L. Jiao, W. Yang, G. Wan, R. Zhang, X. Zheng, H. Zhou, S.-H. Yu and H.-L. Jiang, *Angew. Chem., Int. Ed.*, 2020, **59**, 20589–20595.
200 F. O. Ochedi, D. Liu, J. Yu, A. Hussain and Y. Liu, *Environ. Chem. Lett.*, 2020, **19**, 941–967.
201 W. Ren, X. Tan, W. Yang, C. Jia, S. Xu, K. Wang, S. C. Smith and C. Zhao, *Angew. Chem., Int. Ed.*, 2019, **58**, 6972–6976.
202 J.-H. Guo, X.-Y. Zhang, X.-Y. Dao and W.-Y. Sun, *ACS Appl. Nano Mater.*, 2020, **3**, 2625–2635.
203 Y. Zhang, T. Sun, P. Zhang, K. Liu, F. Li and L. Xu, *J. Colloid Interface Sci.*, 2023, **631**, 96–101.
204 Z. Geng, Y. Cao, W. Chen, X. Kong, Y. Liu, T. Yao and Y. Lin, *Appl. Catal., B*, 2019, **240**, 234–240.
205 L. Lin, H. Li, C. Yan, H. Li, R. Si, M. Li, J. Xiao, G. Wang and X. Bao, *Adv. Mater.*, 2019, **31**, 1903470.
206 G. Chen, H. Zhong and X. Feng, *Chem. Sci.*, 2021, **12**, 15802–15820.
207 H. Xu, D. Cheng, D. Cao and X. C. Zeng, *Nat. Catal.*, 2018, **1**, 339–348.
208 Y. Li, S. L. Zhang, W. Cheng, Y. Chen, D. Luan, S. Gao and X. W. Lou, *Adv. Mater.*, 2022, **34**, 2105204.
209 D. A. Carter and J. E. Pemberton, *J. Raman Spectrosc.*, 1997, **28**, 939–946.
210 J. Wu, M. Liu, P. P. Sharma, R. M. Yadav, L. Ma, Y. Yang, X. Zou, X.-D. Zhou, R. Vajtai and B. I. Yakobson, *Nano Lett.*, 2016, **16**, 466–470.
211 C. Yan, Y. Ye, L. Lin, H. Wu, Q. Jiang, G. Wang and X. Bao, *Catal. Today*, 2019, **330**, 252–258.
212 W. Ju, A. Bagger, G.-P. Hao, A. S. Varela, I. Sinev, V. Bon, B. R. Cuenya, S. Kaskel, J. Rossmeisl and P. Strasser, *Nat. Commun.*, 2017, **8**, 1–9.
213 T. Zheng, K. Jiang, N. Ta, Y. Hu, J. Zeng, J. Liu and H. Wang, *Joule*, 2019, **3**, 265–278.
214 T. Möller, W. Ju, A. Bagger, X. Wang, F. Luo, T. N. Thanh, A. S. Varela, J. Rossmeisl and P. Strasser, *Energy Environ. Sci.*, 2019, **12**, 640–647.

 This journal is © The Royal Society of Chemistry 2024

Published on 25 August 2024. Downloaded on 02.05.26 08:00:32.

215 C. F. Wen, F. Mao, Y. Liu, X. Y. Zhang, H. Q. Fu, L. Zheng, P. F. Liu and H. G. Yang, *ACS Catal.*, 2020, **10**(2), 1086–1093.
216 R. Daiyan, X. Lu, X. Tan, X. Zhu, R. Chen, S. C. Smith and R. Amal, *ACS Appl. Energy Mater.*, 2019, **2**, 8002–8009.
217 C. Yan, H. Li, Y. Ye, H. Wu, F. Cai, R. Si, J. Xiao, S. Miao, S. Xie and F. Yang, *Energy Environ. Sci.*, 2018, **11**, 1204–1210.
218 Y. Li, F. Cui, M. B. Ross, D. Kim, Y. Sun and P. Yang, *Nano Lett.*, 2017, **17**, 1312–1317.
219 O. A. Baturina, Q. Lu, M. A. Padilla, L. Xin, W. Li, A. Serov, K. Artyushkova, P. Atanassov, F. Xu and A. Epshteyn, *ACS Catal.*, 2014, **4**, 3682–3695.
220 K. Shen, X. Chen, J. Chen and Y. Li, *ACS Catal.*, 2016, **6**, 5887–5903.
221 Q. Li, W. Zhu, J. Fu, H. Zhang, G. Wu and S. Sun, *Nano Energy*, 2016, **24**, 1–9.
222 Y.-S. Cheng, X.-P. Chu, M. Ling, N. Li, K.-L. Wu, F.-H. Wu, H. Li, G. Yuan and X.-W. Wei, *Catal. Sci. Technol.*, 2019, **9**, 5668–5675.
223 X. Xuan, J. Cheng, X. Yang and J. Zhou, *ACS Sustain. Chem. Eng.*, 2020, **8**, 1679–1686.
224 S. Zhang, C. Chen, K. Li, H. Yu and F. Li, *J. Mater. Chem. A*, 2021, **9**, 18785–18792.
225 D. Geng, S. Yang, Y. Zhang, J. Yang, J. Liu, R. Li, T.-K. Sham, X. Sun, S. Ye and S. Knights, *Appl. Surf. Sci.*, 2011, **257**, 9193–9198.
226 H. Wang, X. Wu, G. Liu, S. Wu and R. Xu, *Nano Res.*, 2022, 1–8.
227 H. Kiuchi, R. Shibuya, T. Kondo, J. Nakamura, H. Niwa, J. Miyawaki, M. Kawai, M. Oshima and Y. Harada, *Nanoscale Res. Lett.*, 2016, **11**, 1–7.
228 B. Kumar, M. Asadi, D. Pisasale, S. Sinha-Ray, B. A. Rosen, R. Haasch, J. Abiade, A. L. Yarin and A. Salehi-Khojin, *Nat. Commun.*, 2013, **4**, 1–8.
229 J. Wu, R. M. Yadav, M. Liu, P. P. Sharma, C. S. Tiwary, L. Ma, X. Zou, X.-D. Zhou, B. I. Yakobson and J. Lou, *ACS Nano*, 2015, **9**, 5364–5371.
230 H. Wang, J. Jia, P. Song, Q. Wang, D. Li, S. Min, C. Qian, L. Wang, Y. F. Li and C. Ma, *Angew. Chem., Int. Ed.*, 2017, **56**, 7847–7852.
231 S. Zhang, P. Kang, S. Ubnoske, M. K. Brennaman, N. Song, R. L. House, J. T. Glass and T. J. Meyer, *J. Am. Chem. Soc.*, 2014, **136**, 7845–7848.
232 J. Xu, Y. Kan, R. Huang, B. Zhang, B. Wang, K. H. Wu, Y. Lin, X. Sun, Q. Li and G. Centi, *ChemSusChem*, 2016, **9**, 1085–1089.
233 S. Liu, H. Yang, X. Huang, L. Liu, W. Cai, J. Gao, X. Li, T. Zhang, Y. Huang and B. Liu, *Adv. Funct. Mater.*, 2018, **28**, 1800499.
234 Y. Liu, S. Chen, X. Quan and H. Yu, *J. Am. Chem. Soc.*, 2015, **137**, 11631–11636.
235 G.-L. Chai and Z.-X. Guo, *Chem. Sci.*, 2016, **7**, 1268–1275.
236 S. Shiva Kumar and V. Himabindu, *Mater. Sci. Energy Technol.*, 2019, **2**, 442–454.
237 H. R. M. Jhong, C. E. Tornow, B. Smid, A. A. Gewirth, S. M. Lyth and P. J. Kenis, *ChemSusChem*, 2017, **10**, 1094–1099.
238 X. Cui, Z. Pan, L. Zhang, H. Peng and G. Zheng, *Adv. Energy Mater.*, 2017, **7**, 1701456.
239 P. P. Sharma, J. Wu, R. M. Yadav, M. Liu, C. J. Wright, C. S. Tiwary, B. I. Yakobson, J. Lou, P. M. Ajayan and X. D. Zhou, *Angew. Chem., Int. Ed.*, 2015, **54**, 13701–13705.
240 M. Jiang, X. Cao, D. Zhu, Y. Duan and J. Zhang, *Electrochim. Acta*, 2016, **196**, 699–707.
241 L. Chai, L. Zhang, X. Wang, L. Xu, C. Han, T.-T. Li, Y. Hu, J. Qian and S. Huang, *Carbon*, 2019, **146**, 248–256.
242 F. Liu, S. Liu, J. Meng, F. Xia, Z. Xiao, Z. Liu, Q. Li, J. Wu and L. Mai, *Nano Energy*, 2020, **73**, 104758.
243 Y. Xu, Q. Li, H. Xue and H. Pang, *Coord. Chem. Rev.*, 2018, **376**, 292–318.
244 K. Manthiram, B. J. Beberwyck and A. P. Alivisatos, *J. Am. Chem. Soc.*, 2014, **136**, 13319–13325.
245 D. Kim, C. S. Kley, Y. Li and P. Yang, *Proc. Natl. Acad. Sci. U.S.A.*, 2017, **114**, 10560–10565.
246 K. Zhao, Y. Liu, X. Quan, S. Chen and H. Yu, *ACS Appl. Mater. Interfaces*, 2017, **9**, 5302–5311.
247 M. Le, M. Ren, Z. Zhang, P. T. Sprunger, R. L. Kurtz and J. C. Flake, *J. Electrochem. Soc.*, 2011, **158**, E45–E49.
248 K. W. Frese, *J. Electrochem. Soc.*, 1991, **138**, 3338–3344.
249 S.-Y. Zhang, Y.-Y. Yang, Y.-Q. Zheng and H.-L. Zhu, *J. Solid State Chem.*, 2018, **263**, 44–51.
250 M. K. Kim, H. J. Kim, H. Lim, Y. Kwon and H. M. Jeong, *Electrochim. Acta*, 2019, **306**, 28–34.
251 J. Liu, L. Peng, Y. Zhou, L. Lv, J. Fu, J. Lin, D. Guay and J. Qiao, *ACS Sustain. Chem. Eng.*, 2019, **7**, 15739–15746.
252 D. D. Zhu, J. L. Liu and S. Z. Qiao, *Adv. Mater.*, 2016, **28**, 3423–3452.
253 C. I. Shaughnessy, D. T. Jantz and K. C. Leonard, *J. Mater. Chem. A*, 2017, **5**, 22743–22749.
254 J. L. DiMeglio and J. Rosenthal, *J. Am. Chem. Soc.*, 2013, **135**, 8798–8801.
255 W. Guo, X. Sun, C. Chen, D. Yang, L. Lu, Y. Yang and B. Han, *Green Chem.*, 2019, **21**, 503–508.
256 M. Peng, S. Ci, P. Shao, P. Cai and Z. Wen, *J. Nanosci. Nanotechnol.*, 2019, **19**, 3232–3236.
257 D. Li, T. Liu, Z. Yan, L. Zhen, J. Liu, J. Wu and Y. Feng, *ACS Appl. Mater. Interfaces*, 2020, **12**, 7030–7037.
258 Z. Zhao, X. He, J. Yi, C. Ma, Y. Cao and J. Qiu, *RSC Adv.*, 2013, **3**, 84–90.
259 Q. Zhu, J. Ma, X. Kang, X. Sun, H. Liu, J. Hu, Z. Liu and B. Han, *Angew. Chem., Int. Ed.*, 2016, **55**, 9012–9016.
260 P. Lamagni, M. Miola, J. Catalano, M. S. Hvid, M. A. H. Mamakhel, M. Christensen, M. R. Madsen, H. S. Jeppesen, X. M. Hu and K. Daasbjerg, *Adv. Funct. Mater.*, 2020, **30**, 1910408.
261 M. Feyand, E. Mugnaioli, F. Vermoortele, B. Bueken, J. M. Dieterich, T. Reimer, U. Kolb, D. De Vos and N. Stock, *Angew. Chem., Int. Ed.*, 2012, **51**, 10373–10376.
262 V. Vivier, A. Regis, G. Sagon, J.-Y. Nedelec, L. Yu and C. Cachet-Vivier, *Electrochim. Acta*, 2001, **46**, 907–914.
263 Z. Ma, D. Wu, X. Han, H. Wang, L. Zhang, Z. Gao, F. Xu and K. Jiang, *J. $CO_2$ Util.*, 2019, **32**, 251–258.
264 W.-H. Li, W.-H. Deng, G.-E. Wang and G. Xu, *EnergyChem*, 2020, **2**, 100029.

265 R. Sakamoto, K. Takada, T. Pal, H. Maeda, T. Kambe and H. Nishihara, *Chem. Commun.*, 2017, **53**, 5781–5801.
266 J. T. Feaster, C. Shi, E. R. Cave, T. Hatsukade, D. N. Abram, K. P. Kuhl, C. Hahn, J. K. Nørskov and T. F. Jaramillo, *ACS Catal.*, 2017, **7**, 4822–4827.
267 J. S. Yoo, R. Christensen, T. Vegge, J. K. Nørskov and F. Studt, *ChemSusChem*, 2016, **9**, 358–363.
268 J. M. Barlow and J. Y. Yang, *ACS Cent. Sci.*, 2019, **5**, 580–588.
269 Q. Fan, P. Hou, C. Choi, T. S. Wu, S. Hong, F. Li, Y. L. Soo, P. Kang, Y. Jung and Z. Sun, *Adv. Energy Mater.*, 2020, **10**, 1903068.
270 Y. R. Wang, Q. Huang, C. T. He, Y. Chen, J. Liu, F. C. Shen and Y. Q. Lan, *Nat. Commun.*, 2018, **9**, 4466.
271 E. Zhang, T. Wang, K. Yu, J. Liu, W. Chen, A. Li, H. Rong, R. Lin, S. Ji and X. Zheng, *J. Am. Chem. Soc.*, 2019, **141**, 16569–16573.
272 Z. Zhang, J. Xiao, X. J. Chen, S. Yu, L. Yu, R. Si, Y. Wang, S. Wang, X. Meng and Y. Wang, *Angew. Chem., Int. Ed.*, 2018, **57**, 16339–16342.
273 N. Kornienko, Y. Zhao, C. S. Kley, C. Zhu, D. Kim, S. Lin, C. J. Chang, O. M. Yaghi and P. Yang, *J. Am. Chem. Soc.*, 2015, **137**, 14129–14135.
274 H. Zhong, M. Ghorbani-Asl, K. H. Ly, J. Zhang, J. Ge, M. Wang, Z. Liao, D. Makarov, E. Zschech, E. Brunner, I. M. Weidinger, J. Zhang, A. V. Krasheninnikov, S. Kaskel, R. Dong and X. Feng, *Nat. Commun.*, 2020, **11**, 1409.
275 R. Iqbal, M. B. Akbar, A. Ahmad, A. Hussain, N. Altaf, S. Ibraheem, G. Yasin, M. A. Khan, M. Tabish and A. Kumar, *Adv. Mater. Interfaces*, 2022, **9**, 2101505.

Published on 25 August 2024. Downloaded on 02.05.26 08:00:32.


This journal is © The Royal Society of Chemistry 2024